Cell

Peroxisomes Are Signaling Platforms for Antiviral Innate Immunity

Evelyn Dixit,[1,2] Steeve Boulant,[3] Yijing Zhang,[1] Amy S.Y. Lee,[3,4] Charlotte Odendall,[1] Bennett Shum,[5] Nir Hacohen,[5] Zhijian J. Chen,[6,7] Sean P. Whelan,[3,4] Marc Fransen,[8] Max L. Nibert,[3,4] Giulio Superti-Furga,[2] and Jonathan C. Kagan[1,*]
[1]Harvard Medical School and Division of Gastroenterology, Children's Hospital Boston, Boston, MA 02115, USA
[2]CeMM-Research Center for Molecular Medicine of the Austrian Academy of Sciences, 1090 Vienna, Austria
[3]Department of Microbiology and Molecular Genetics, Harvard Medical School, Boston, MA 02115, USA
[4]Training Program in Virology, Division of Medical Sciences, Harvard University, Boston, MA 02115, USA
[5]Broad Institute of MIT and Harvard, Cambridge, MA 02142, USA
[6]Department of Molecular Biology
[7]Howard Hughes Medical Institute
University of Texas Southwestern Medical Center, Dallas, TX 75390, USA
[8]Katholieke Universiteit Leuven, Faculteit Geneeskunde, Departement Moleculaire Celbiologie, LIPIT, Campus Gasthuisberg (O&N 1), 3000 Leuven, Belgium
*Correspondence: jonathan.kagan@childrens.harvard.edu
DOI 10.1016/j.cell.2010.04.018

SUMMARY

Peroxisomes have long been established to play a central role in regulating various metabolic activities in mammalian cells. These organelles act in concert with mitochondria to control the metabolism of lipids and reactive oxygen species. However, while mitochondria have emerged as an important site of antiviral signal transduction, a role for peroxisomes in immune defense is unknown. Here, we report that the RIG-I-like receptor (RLR) adaptor protein MAVS is located on peroxisomes and mitochondria. We find that peroxisomal and mitochondrial MAVS act sequentially to create an antiviral cellular state. Upon viral infection, peroxisomal MAVS induces the rapid interferon-independent expression of defense factors that provide short-term protection, whereas mitochondrial MAVS activates an interferon-dependent signaling pathway with delayed kinetics, which amplifies and stabilizes the antiviral response. The interferon regulatory factor IRF1 plays a crucial role in regulating MAVS-dependent signaling from peroxisomes. These results establish that peroxisomes are an important site of antiviral signal transduction.

INTRODUCTION

A fundamental feature of eukaryotic cells is the use of membrane-bound organelles to compartmentalize activities and serve as scaffolds for signal transduction. The best-characterized signaling pathways involve membrane-bound receptors that respond to extracellular or lumenal stimuli. In these instances, the spatial separation of an extracellular stimulus from the cytosol mandates the use of organelles as signaling platforms, as transmembrane receptors must transmit information across a lipid bilayer. However, an important gap exists in our knowledge of how stimuli from the cytosol are able to initiate specific signaling events.

How common is the use of organelles in signal transduction from cytosolic receptors? An example of this situation can be found in the study of virus-host interactions. The ability to detect cytosolic viruses depends on the RIG-I-like receptor (RLR) family of proteins, which are soluble RNA helicases that detect viruses containing RNA (and in some cases DNA) genomes (Ablasser et al., 2009; Chiu et al., 2009; Yoneyama et al., 2004). The best characterized RLRs, RIG-I and MDA-5, detect 5′-triphosphate-containing short double-stranded RNA (dsRNA) and long dsRNA, respectively (Kato et al., 2008; Pichlmair et al., 2006). RLRs can either detect viral RNA directly or after RNA polymerase III-mediated transcription of microbial DNA (Ablasser et al., 2009; Chiu et al., 2009; Kato et al., 2008). Mice deficient in either of these RLRs are sensitive to different classes of viruses, underscoring both their specificity of action and their importance in immune defense (Gitlin et al., 2006; Kato et al., 2006).

Although RIG-I and MDA-5 have specificities for different ligands, both induce a common signaling pathway that triggers the expression of type I interferons (IFNs) and IFN-stimulated genes (ISGs). Many ISGs function as direct antiviral effectors, acting to prevent viral genome replication, viral particle assembly, or virion release from infected cells. Generally, it is thought that RLRs induce the expression of IFNs that act in both autocrine and paracrine manners to amplify ISG expression. However, ISGs can also be induced directly upon viral infection, without the need for IFN signaling (Collins et al., 2004; Mossman et al., 2001). At the receptor-proximal level, RLR-dependent responses are regulated by the adaptor protein MAVS (also called IPS-1, Cardif, or VISA) (Nakhaei et al., 2009). Upon viral detection, MAVS binds to RLRs and promotes the activation of NF-κB, AP-1, and various interferon regulatory factors (IRFs), which act to induce ISGs and create an antiviral state in the cell. Although much has been learned about the genetics of RLR signaling, less is known about where within

the cell signal transduction occurs. Identifying the sites of RLR signal transduction is critical to understanding how antiviral networks are integrated into the general cellular infrastructure within which they operate.

The first clue that cytosolic RLR signaling may occur from organelles came from studies of the MAVS adaptor. MAVS contains a C-terminal transmembrane domain that anchors it to the mitochondrial outer membrane (Seth et al., 2005). It is from this location that MAVS is thought to engage active RLRs and induce signal transduction. Whether mitochondria are the only organelles that promote RLR-mediated signaling has not been addressed.

Mitochondria have long been appreciated to have an intimate functional relationship with peroxisomes (Hettema and Motley, 2009). Both are membrane-bound organelles found in mammalian cells and are involved in the metabolism of lipids and reactive oxygen species. However, while mitochondria are well-established sites of both antiviral signaling and antiviral apoptosis, peroxisomes are thought to function solely as metabolic organelles.

Recently, several mitochondrial proteins have been found to reside also on peroxisomes. Included in this group are the outer membrane proteins Fis1 and Mff, which regulate the morphology of both organelles (Gandre-Babbe and van der Bliek, 2008; Koch et al., 2005). Interestingly, Fis1, Mff, and MAVS all have similar domain structures: each contains an N-terminal effector domain and a C-terminal localization motif, which consists of a transmembrane domain and a short lumenal tail containing basic amino acids. That other so-called ''tail-anchored'' mitochondrial outer membrane proteins operate from peroxisomes raised the possibility that MAVS also functions from these organelles.

We have discovered that MAVS does indeed reside on peroxisomes and can induce antiviral signaling from this organelle. Our work supports a model whereby peroxisomal MAVS induces the immediate expression of antiviral factors that function to contain a nascent infection. Long-term containment of the infection, however, requires the function of mitochondrial MAVS as well. These data demonstrate that peroxisomes are not simply metabolic organelles, but rather serve as critical subcellular hubs that promote MAVS-dependent antiviral immunity.

RESULTS

MAVS Is Located on Both Mitochondria and Peroxisomes

MAVS has a similar domain organization to other tail-anchored membrane proteins that function from mitochondria and peroxisomes (Gandre-Babbe and van der Bliek, 2008; Koch et al., 2005). We therefore sought to determine whether MAVS also resides on peroxisomes. The subcellular localization of MAVS was examined in mouse embryonic fibroblasts (MEFs) whose peroxisomes were marked by a DsRed allele containing a type 1 peroxisomal targeting signal (PTS1). In addition to staining structures that appeared to be mitochondria, MAVS was detected on PTS1-positive peroxisomes scattered throughout the cell (Figure 1A). A similar staining pattern was seen for Mff (Figure 1A), which functions from both peroxisomes and mitochondria (Gandre-Babbe and van der Bliek, 2008). In contrast, the Toll-like receptor (TLR) adaptor protein TIRAP (Fitzgerald et al., 2001; Horng et al., 2001) was not detected on peroxisomes (Figure 1A). To confirm that the peroxisomal staining was distinct from mitochondria, we also stained cells with MitoTracker. Although no costaining was detected between PTS1 and MitoTracker, MAVS was detected on both PTS1-positive peroxisomes and MitoTracker-positive mitochondria (Figure 1B). Similar results were obtained when epitope-tagged MAVS in murine macrophages (Figure S1 available online) or endogenous MAVS in human hepatocytes were examined (Figure 1C). As an independent means of assessing MAVS localization, hepatocytes were biochemically fractionated to separate peroxisomes and mitochondria, which were respectively distinguished by Pex14 and mtHSP70 (Figure 1D). Both MAVS and Fis1 (a protein that occupies both organelles [Koch et al., 2005]) were detected in fractions containing either peroxisomes or mitochondria. Collectively, on the basis of studies in both human and mouse cells, these data establish that peroxisomes are a bona fide reservoir of the RLR adaptor protein MAVS.

One possible reason MAVS is present on peroxisomes is that newly synthesized MAVS might first pass through peroxisomes en route to mitochondria. To address this possibility, we used human fibroblasts from a patient lacking a functional Pex19 protein. Pex19 controls peroxisome biogenesis, and thus Pex19-deficient cells contain no peroxisomes or peroxisomal remnant structures (Matsuzono et al., 1999; Sacksteder et al., 2000). Notably, MAVS was delivered to mitochondria in Pex19-deficient cells (Figure 1E), indicating that the pathway to mitochondria does not require a peroxisomal intermediate. Moreover, MAVS localized to both peroxisomes and mitochondria in Pex19-deficient cells that expressed Pex19 after transient transfection or retroviral gene transfer (Figure 1E). It is therefore unlikely that localization of MAVS to peroxisomes is the result of a biosynthetic pathway for delivering outer membrane proteins to mitochondria.

A Systematic Strategy to Separate Functions of Peroxisomal and Mitochondrial MAVS

Our finding that MAVS is located on peroxisomes raised the possibility that these organelles serve as a site of antiviral signal transduction. We first considered using Pex19-deficient cells to address sufficiency of mitochondrial MAVS in antiviral signaling, but since peroxisomes are required for biochemical processes that occur in mitochondria, Pex19-deficient cells have profound defects in mitochondrial function (Wanders, 2004). We therefore used the alternative approach of genetically separating the putative mitochondrial and peroxisomal functions of MAVS. This was accomplished by replacing the previously defined MAVS localization motif (Seth et al., 2005) with a set of domains that instead direct the protein to a single compartment (Figure 2A). Using the localization motif of the peroxin Pex13 (Fransen et al., 2001), we created a protein called MAVS-Pex. By deleting the MAVS localization motif, we also created a cytosolic allele (MAVS-Cyto) (Seth et al., 2005). Because the fidelity of mitochondrial sorting signals is not always transferrable to other proteins (Ingelmo-Torres et al., 2009), we lastly created two different alleles of MAVS containing a sorting signal derived from two proteins residing on the mitochondrial outer membrane protein, either OMP25 or Fis1 (Koch et al., 2005; Nemoto and De Camilli, 1999).

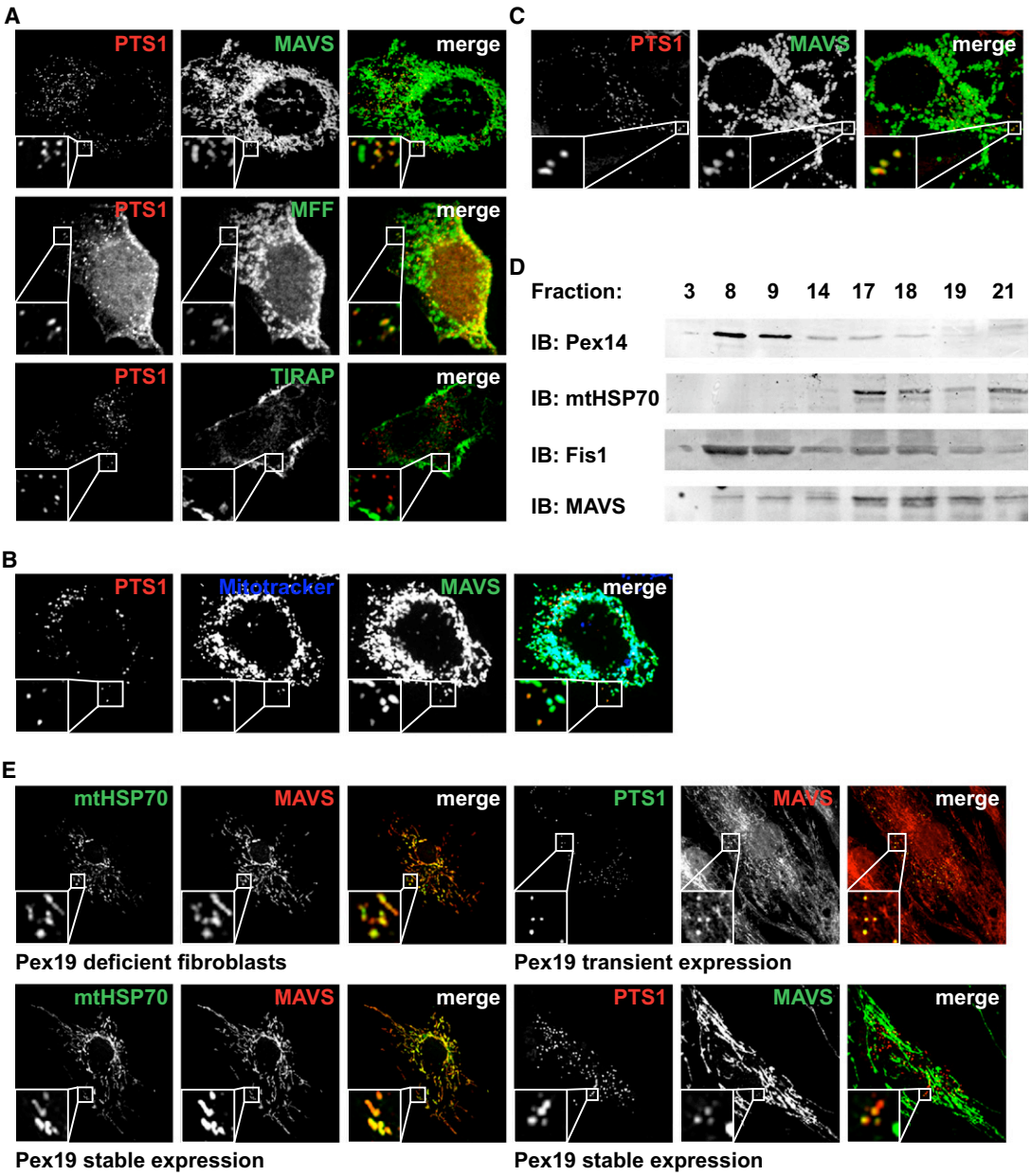

Figure 1. MAVS resides on mitochondria and peroxisomes

(A) MEFs were transfected with the peroxisomal marker DsRed-PTS1 and Flag-MAVS, myc-MFF, or Flag-TIRAP. Cells were stained with anti-MAVS, anti-myc, or anti-Flag antibodies, respectively. All images for all panels are representative of at least three independent experiments in which over 500 cells were examined per condition and >95% of the cells displayed similar staining.

(B) MEFs expressing Flag-MAVS as well as EGFP-PTS1 and Pex19 from a bicistronic construct were stained with anti-MAVS antibody and MitoTracker to visualize mitochondria.

(C) Huh-7 hepatocytes were transfected with DsRed-PTS1 and endogenous MAVS was detected with anti-MAVS antisera.

(D) Peroxisomes were separated from mitochondria on a Nycodenz gradient with HepG2 hepatocyte lysates. Selected fractions of the gradient were analyzed by immunoblotting with Pex14, mtHSP70, Fis1, or MAVS antisera.

(E) Pex19-deficient human fibroblasts were stained for endogenous MAVS before and after introduction of a functional Pex19 allele as indicated. Mitochondria were stained with anti-mtHSP70 antibody. Peroxisomes were visualized by transfection with a bicistronic construct encoding EGFP-PTS1 and Pex19.

See also Figure S1.

Using retroviral gene transfer of MAVS-KO MEFs, we created cell lines expressing comparable levels of each MAVS allele (Figures 2B and 2C) and determined their localizations by confocal microscopy. Full-length MAVS (MAVS-WT) was located on both mitochondria and peroxisomes (data not shown), and MAVS-Cyto was found on neither organelle (Figure 2D and

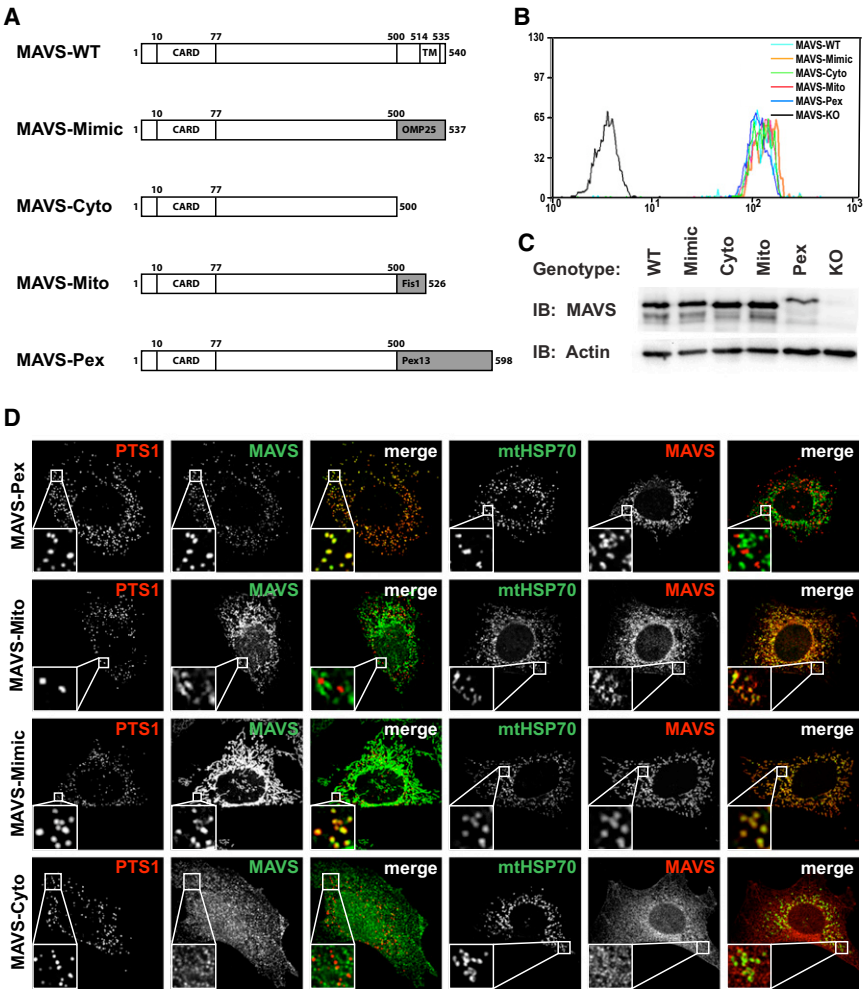

Figure 2. Targeting of MAVS to Distinct Subcellular Compartments by Replacement of Its Transmembrane Domain

(A) Schematic of WT and mutant MAVS alleles to be tested for signaling from peroxisomes and mitochondria.

(B) Stable cell lines expressing the MAVS alleles listed in (A) were generated by retroviral transduction of MAVS-KO cells. Resulting transgenic cells expressed a MAVS allele and GFP, whose translation is directed by an IRES. Shown are overlaid histograms of stable populations of each cell line expressing equivalent levels of the bicistronic mRNAs encoding MAVS and GFP.

(C) Lysates from stable cell lines described in (B) and parental MAVS KO MEFs were analyzed by immunoblotting with anti-MAVS antibody.

(D) Micrographs of MAVS chimeric cell lines indicated were stained with anti-MAVS antibody. Mitochondria were stained with anti-mtHSP70 antibody. Peroxisomes were visualized by transfection with DsRed-PTS1. Note that MAVS-Pex resides on peroxisomes, MAVS-Mito on mitochondria, MAVS-Mimic on both organelles, and MAVS-Cyto localizes on neither of the two organelles. All images for all panels are representative of at least three independent experiments where over 500 cells were examined per condition and >95% of the cells displayed similar staining.

See also Figure S2.

Figure S2). As expected, MAVS-Pex was found exclusively on peroxisomes (Figure 2D and Figure S2). Of the alleles containing the putative mitochondrial targeting sequences, the allele harboring the Fis1 transmembrane domain was found primarily on mitochondria, whereas the one containing the OMP25 transmembrane domain was located on both mitochondria and peroxisomes (Figure 2D and Figure S2). We therefore refer to the mitochondria-specific allele as MAVS-Mito to indicate its exclusive localization to mitochondria and the allele found on both organelles as MAVS-Mimic to indicate its ability to copy the localization pattern of MAVS-WT. Collectively, this set of MAVS-expressing MEF lines differs only in the subcellular positioning of the signaling domain of MAVS and thereby provides an ideal system to determine the relative roles of mitochondrial and peroxisomal localization in MAVS-dependent signal transduction.

MAVS-Dependent Signaling Occurs from Both Peroxisomes and Mitochondria

To address the function of peroxisomal MAVS, we monitored the expression of antiviral factors in response to infection with reovirus. We chose reovirus because it is a known inducer of both RIG-I and MDA-5 signaling pathways (Loo et al., 2008), allowing direct examination of both RLRs in a single experiment.

Cells were infected with reovirus, and extracts were examined at various times for expression of viperin, a well-characterized ISG (Chin and Cresswell, 2001; Severa et al., 2006). MAVS-WT-, -Mimic-, or -Mito-expressing cells induced viperin expression in response to infection (Figure 3A). This response was MAVS dependent, as MAVS-KO cells showed no change in viperin expression. MAVS-Cyto cells were unable to induce viperin expression, confirming that membrane localization is necessary for MAVS function (Seth et al., 2005). Interestingly, despite the fact that MAVS-Pex is found only on peroxisomes, MAVS-Pex cells induced viperin expression after infection (Figure 3A).

An examination of the kinetics of ISG induction indicated that cells containing MAVS on peroxisomes (MAVS-WT, -Mimic, and -Pex) induced viperin expression within 4 hr of infection. In contrast, exclusive localization to mitochondria (MAVS-Mito) resulted in viperin expression with delayed kinetics (Figure 3A). These results suggest that localization of MAVS to either peroxisomes or mitochondria is sufficient to induce antiviral signaling but that peroxisomal residence allows for more rapid expression of ISGs. Interestingly, rapid expression of ISGs by MAVS-Pex appeared to be transient, as viperin expression decreased at later times of infection (Figure 3A).

To determine whether peroxisomal signaling by MAVS requires signaling by both RIG-I and MDA-5, we performed

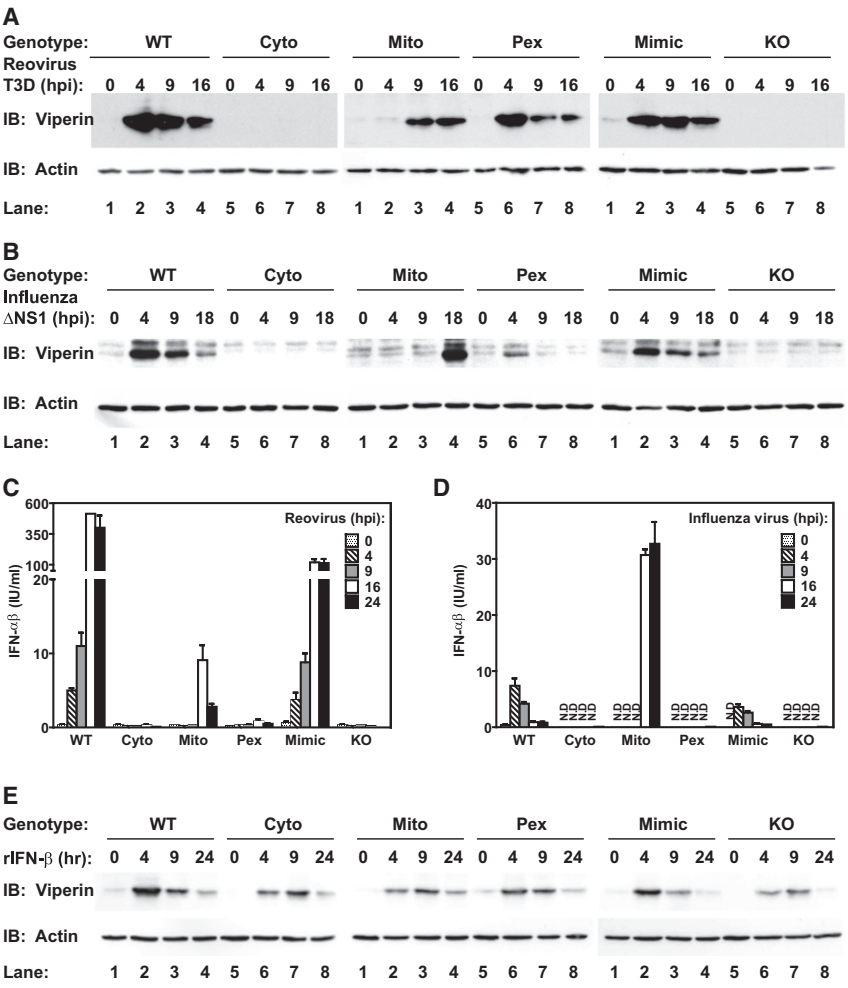

Figure 3. Peroxisomal MAVS Mediates ISG Expression, but Does Not Induce Type I IFN Secretion

(A) MAVS-expressing MEFs and MAVS-KO cells were infected with reovirus. At indicated times, cell-associated ISG expression was determined by immunoblotting with an anti-viperin antibody.

(B) Similar to (A) except for infection with influenza virus strain ΔNS1 in lieu of reovirus.

(C and D) Cell culture media from (A) and (B) were tested for type I IFN activity using a bioassay. Error bars show the standard deviation of triplicate infections.

(E) MAVS-expressing MEFs and parental MAVS-KO cells were treated with 100 IU/ml IFNβ. At indicated times, cell-associated ISG expression was determined by immunoblotting with anti-viperin antibody. Note that all cell lines respond similarly to IFNβ, indicating intact type I IFN signaling.

All data are the result of at least two independent experiments. See also Figure S3.

similar experiments using influenza virus, which activates the RIG-I pathway exclusively (Gitlin et al., 2006; Kato et al., 2006). A similar pattern of viperin expression was observed with influenza as with reovirus, although the kinetic differences between MAVS-Pex and -Mito were even more pronounced with influenza (Figure 3B). Thus, RIG-I signaling alone is sufficient to induce MAVS-dependent signaling from peroxisomes. In sum, these data indicate that peroxisomal MAVS induces rapid but transient viperin expression, whereas mitochondrial MAVS induces delayed but stable viperin expression. Signaling from both organelles thus contributes to the rapid and stable expression of viperin that is observed in MAVS-WT cells.

While the above studies provide strong genetic evidence for MAVS signaling from peroxisomes in a population of cells, they do not allow us to examine individual cells for compartment-specific signaling events. To address this, we took advantage of the fact that various signaling pathways induce morphological changes in the organelles where signaling occurs, including RLR-dependent activities on mitochondria (Castanier et al., 2010; Yasukawa et al., 2009). We reasoned that if signaling was actually occurring on these organelles, then their morphology may change during viral infection. In support of this prediction, reovirus infection induced peroxisomal aggregation and the formation of peroxisomal tubules (Figures S3A and S3B). The tubes formed ranged from approximately 2 μm in length to over 5 μm and depended on MAVS localization to peroxisomes. Cells expressing MAVS-WT exhibited this activity, and cells expressing MAVS-Pex have greatly exaggerated behavior in these assays, with nearly all cells displaying peroxisomes over 5 μm in length (Figures S3A and S3B). Cells expressing MAVS-Mito or MAVS-Cyto exhibited little or no change in peroxisome morphology. These data suggest that RLRs engage peroxisomal MAVS to induce peroxisomal tubules and that the extent of tubulation is determined by the concentration of MAVS on these organelles. These independent assays demonstrate that MAVS-dependent signaling occurs locally (on the peroxisome).

Peroxisomal MAVS Triggers an IFN-Independent Signaling Pathway that Promotes ISG Expression

The different kinetics of viperin induction by peroxisomal and mitochondrial MAVS suggest that more than one mechanism of RLR-induced ISG expression may operate in virus-infected cells. ISG expression can be induced directly, or it can be induced indirectly through the action of secreted type I IFNs (Collins et al., 2004; Mossman et al., 2001). To determine whether IFNs contribute to expression of ISGs induced by mitochondrial or peroxisomal MAVS, we monitored the rate of IFN production by reovirus-infected cells. As expected, IFN production was dependent on membrane-localized MAVS, and all mitochondrial MAVS proteins (MAVS-WT, -Mimic, and -Mito) triggered IFN production, though with delayed kinetics in the case of MAVS-Mito (Figure 3C). These data indicate that in the case of the mitochondria-localized MAVS proteins, IFN

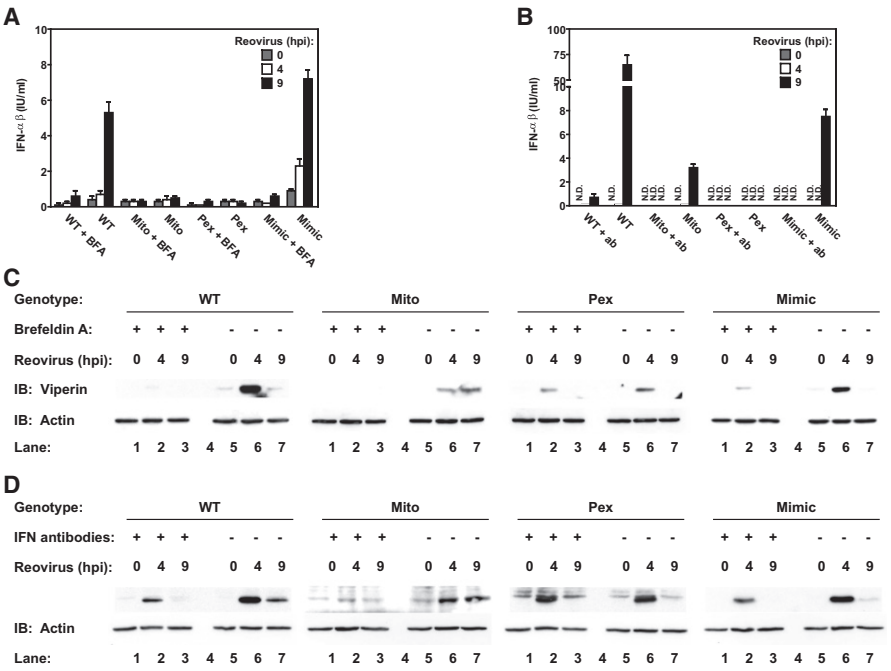

Figure 4. Peroxisomal MAVS Directly Induces Viperin Expression

(A) MAVS-expressing MEFs and MAVS-KO cells were pretreated with 20 μg/ml BFA before infection with reovirus in presence of the drug. At indicated times, cell supernatants were tested for type I IFN activity via a bioassay.

(B) Similar to (A) except type I IFN activity was blocked by addition of 250 NU/ml anti-IFNβ and 500 NU/ml anti-IFNα antibodies after infection with reovirus.

(C and D) Cell lysates from (A) and (B) were tested for ISG expression by immunoblotting with anti-viperin antibody. Note that IFN activity is not required for viperin expression mediated by peroxisomal MAVS.

All data are the representative of at least three independent experiments. Error bars show standard deviation of triplicate infections.

expression coincides with ISG induction. Surprisingly, no detectable IFNs were produced by MAVS-Pex cells. Similar results were obtained with cells infected with influenza virus (Figure 3D), though the relative amounts of IFNs produced with these two viruses differed dramatically, reflecting unique aspects of each virus life cycle. However, our inability to detect a role for IFNs in promoting viperin expression in MAVS-Pex cells was not due to an inability of the cells to respond to IFNs, because addition of recombinant IFNβ was sufficient to induce viperin expression in all cells examined (Figure 3E).

The observation that viperin can be expressed in the absence of type I IFN induction suggests that IFNs may not contribute to ISG expression induced by peroxisomal MAVS. We tested this possibility by infecting cells under conditions in which the functions of IFNs are prevented, by either disrupting protein secretion with brefeldin A (BFA) or by utilizing neutralizing antibodies against secreted IFNs. Both treatments disrupted the activity of type I IFNs produced during reovirus infection (Figures 4A and 4B) and inhibited the expression of viperin by cells expressing mitochondrial MAVS (MAVS-WT, -Mimic, and -Mito) (Figures 4C and 4D). These data indicate that signaling by IFNs promotes viperin expression. However, because these treatments did not completely abolish viperin expression, an IFN-independent pathway of viperin induction must also exist. Interestingly, MAVS signaling from peroxisomes primarily utilized the IFN-independent pathway, as viperin expression within MAVS-Pex cells was largely resistant to these treatments (Figures 4C and 4D). These data therefore indicate that the subcellular positioning of MAVS determines the type of signaling pathway activated during viral infection. Peroxisomal MAVS induces the rapid and direct expression of viperin, which is followed by mitochondrial MAVS triggering viperin expression directly, as well as indirectly through the IFN-mediated feed-forward loop.

The Global Transcriptional Response to Reovirus Infection Is Mediated by the Collective Actions of MAVS-Dependent Peroxisomal and Mitochondrial Signaling

Based on the set of candidate genes examined, our data suggests that peroxisomal and mitochondrial MAVS each induce a complementary set of genes that are collectively induced by MAVS-WT. To determine whether this is the case, microarrays were performed on reovirus-infected cells. Infections were performed for 3, 9, or 16 hr, and RNA was collected for genome-wide expression analysis. At all times examined, similar expression profiles were observed when MAVS-WT and MAVS-Mimic cells were compared, confirming that similarities in MAVS localization are predictive of similarities in MAVS function (Figures 5A and 5B). These cells induced the expression of numerous ISGs, IFNs, and chemokines (Figure 5C). Notably, we were unable to detect the expression of the proinflammatory cytokines TNFα, IL-1β, or IL-6 (data not shown). MAVS-Cyto cells were most

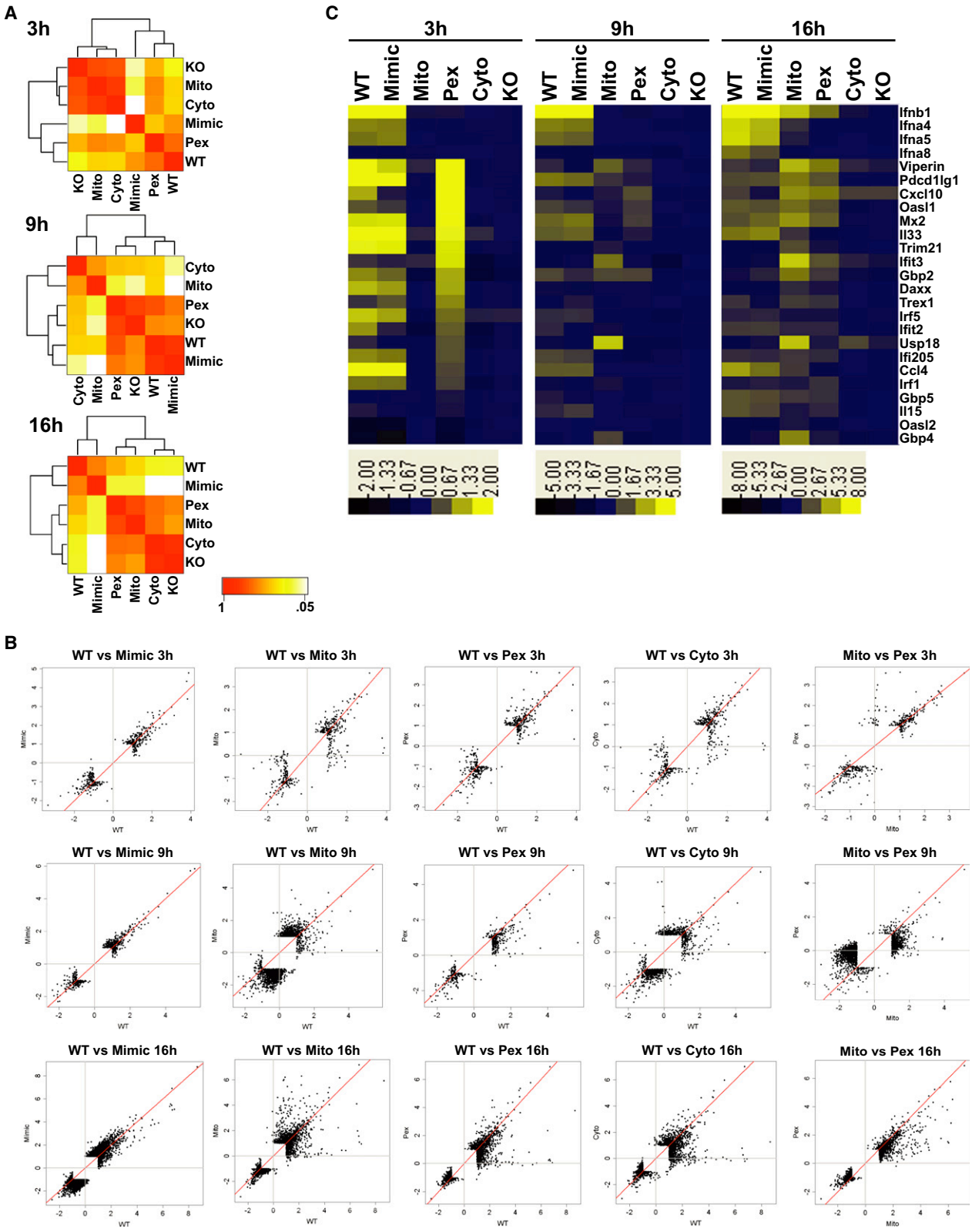
A
3h
KO
Mito
Cyto
Mimic
Pex
WT
9h
Cyto
Mito
Pex
KO
WT
Mimic
16h
WT
Mimic
Pex
Mito
Cyto
KO
1
.05
C
3h
9h
16h
WT
Mimic
Mito
Pex
Cyto
KO
Ifnb1
Ifna4
Ifna5
Ifna8
Viperin
Pdcd1lg1
Cxcl10
Oasl1
Mx2
Il33
Trim21
Ifit3
Gbp2
Daxx
Trex1
Irf5
Ifit2
Usp18
Ifi205
Ccl4
Irf1
Gbp5
Il15
Oasl2
Gbp4
-2.00 -1.33 -0.67 0.00 0.67 1.33 2.00
-5.00 -3.33 -1.67 0.00 1.67 3.33 5.00
-8.00 -5.33 -2.67 0.00 2.67 5.33 8.00
B
WT vs Mimic 3h
WT vs Mito 3h
WT vs Pex 3h
WT vs Cyto 3h
Mito vs Pex 3h
WT vs Mimic 9h
WT vs Mito 9h
WT vs Pex 9h
WT vs Cyto 9h
Mito vs Pex 9h
WT vs Mimic 16h
WT vs Mito 16h
WT vs Pex 16h
WT vs Cyto 16h
Mito vs Pex 16h

similar to MAVS-KO cells (Figures 5A and 5B), further confirming that membrane localization of MAVS is critical for its function in antiviral signaling. Interestingly, MAVS-Pex- or -Mito-expressing cells displayed a transcriptome that each partially overlapped with that of MAVS-WT cells, but were distinct from one another (Figures 5B and 5C). For example, at 16 hr after infection, MAVS-Mito cells upregulated genes encoding chemokines, ISGs, IFNβ, and several IFNα family members (Figures 5B and 5C). MAVS-Pex cells also induced the expression of chemokines and ISGs, but without any detectable changes in IFN expression and with much faster kinetics (within 3 hr). Thus, on a global scale, peroxisomal MAVS induces the rapid expression of ISGs without inducing IFN expression, whereas mitochondrial MAVS promotes IFN and ISG expression but with delayed kinetics. We confirmed these results by examining the expression of several candidate IFNs and ISGs using nCounter, which allows for multiplex analysis of gene expression with the sensitivity of quantitative RT-PCR (Geiss et al., 2008) (Figures S4A and S4B). Overall, at all times examined, most genes expressed by either peroxisomal or mitochondrial MAVS were induced by MAVS-WT or -Mimic (Figures 5B and 5C). These data therefore support a model whereby the host transcriptional response is the result of MAVS signaling from both mitochondria and peroxisomes. We do note however, that the magnitude of antiviral gene expression induced by cells expressing MAVS-WT or MAVS-Mimic was greater than the magnitude induced by cells where MAVS was restricted to a single organelle, which suggests that signaling from both organelles may be coordinated to ensure maximal antiviral gene expression.

Peroxisomal Signal Transduction Creates a Transient but Functional Antiviral State

MAVS-dependent signaling promotes an antiviral state, which is functionally defined as the ability of cells to restrict multiplication of viruses. To determine the significance of mitochondrial or peroxisomal signaling pathways in this regard, we asked whether signaling from either organelle is sufficient to restrict viral replication. We addressed this by infecting MAVS-expressing cells with reovirus and measuring production of infectious virions over time. As expected, MAVS-WT and -Mimic cells were most resistant to infection, and MAVS-KO and -Cyto cells were most susceptible (Figure 6A). These data indicate that MAVS signaling is required to limit reovirus replication. Interestingly, cells expressing MAVS-Pex or MAVS-Mito exhibited an unusual biphasic behavior. Over the first 24 hr, these cells restricted viral replication as well as MAVS-WT, but this capacity diminished, and by 72 hr were most similar to the MAVS-KO cells. These data establish that signaling from either peroxisomes or mitochondria is sufficient to induce a functional antiviral response, but signaling from both organelles is necessary for maximal containment of reovirus replication.

Vesicular stomatitis virus (VSV) is one of many viruses that interfere with type I IFN expression as part of their pathogenic lifecycle (Figures 6B and 6C) (Ferran and Lucas-Lenard, 1997). Under these conditions, the IFN-independent means of signaling that is induced by peroxisomal MAVS may be particularly important in controlling infection. Consistent with this idea, MAVS-Mito cells were as susceptible to VSV infection as MAVS-KO or -Cyto cells (Figure 6D), suggesting that in the absence of IFN production, the mitochondrial signaling pathway is functionally defective. Most notably, MAVS-Pex cells were nearly as effective at controlling VSV as MAVS-WT cells (Figure 6D). These results suggest that MAVS signaling from peroxisomes is the primary means of controlling viruses that interfere with IFN expression, thus underscoring the importance of this organelle in host defense.

Downstream Regulators of MAVS Signaling from Peroxisomes

To identify downstream signaling regulators of peroxisomal MAVS, we overexpressed each MAVS allele in 293T human kidney epithelial cells. MAVS-WT, -Mimic, -Mito, and -Pex each induced the activation of reporter genes controlled by NF-κB and AP-1 (Figure 6E). In addition, an IRF1 reporter and an ISRE that typically reports IRF3 activity were induced, suggesting a role of these IRFs in MAVS signaling from peroxisomes (Figure 6E). MAVS-Cyto did not activate any reporter. Within these cells, we found that ISRE activation by either MAVS-WT or MAVS-Pex was potentiated by overexpression of TRAF3 and inhibited by expression of a dominant negative allele of TRAF6 (Figure S5A), suggesting the involvement of these known RLR regulators in peroxisomal signaling (Saha et al., 2006; Yoshida et al., 2008). In contrast, expression of a dominant-negative allele of the antiviral factor FADD has a minimal affect on MAVS signaling (Figure S5A), which is consistent with a recent report (Balachandran et al., 2007). Notably, overexpression of NLRX1, a negative regulator that is uniquely located on mitochondria (Figure S5B) (Moore et al., 2008) did not interfere with MAVS-Pex signaling, but did inhibit signaling by MAVS-WT (Figure S5A).

To confirm the roles of IRF1 and IRF3 in peroxisomal signaling, we enlisted VSV to study the IFN-independent means of ISG expression, since only the peroxisomal pathway functions to control replication of this virus, although some ISGs were

Figure 5. Genome-wide Transcriptome Analysis Reveals a General Role for Peroxisomal and Mitochondrial MAVS in Antiviral Gene Expression

(A) RNA from MAVS-expressing MEFs and parental MAVS-KO cells after infection with reovirus for 3, 9, or 16 hr was subject to microarray analysis. The similarity of the overall gene expression profiles mediated by the indicated MAVS alleles is displayed as Pearson correlation coefficient-based heat map. Samples are clustered along both axes based on their correlation value. Note that at 3 hr after infection, MAVS-Pex cells display a gene expression pattern that is most similar to MAVS-WT cells.

(B) Pairwise comparisons of indicated cell lines based on 4089 significantly regulated genes depicted in a log-log scale scatter plot. Each data point indicates a gene whose expression level exhibited a change of greater than 2-fold.

(C) Heat map of selected genes based on their expression ratios across all six cell lines and during all time points upon reovirus infection.

Genes are colored according to a log2-based color bar depicted underneath each heat map. See also Figure S4.

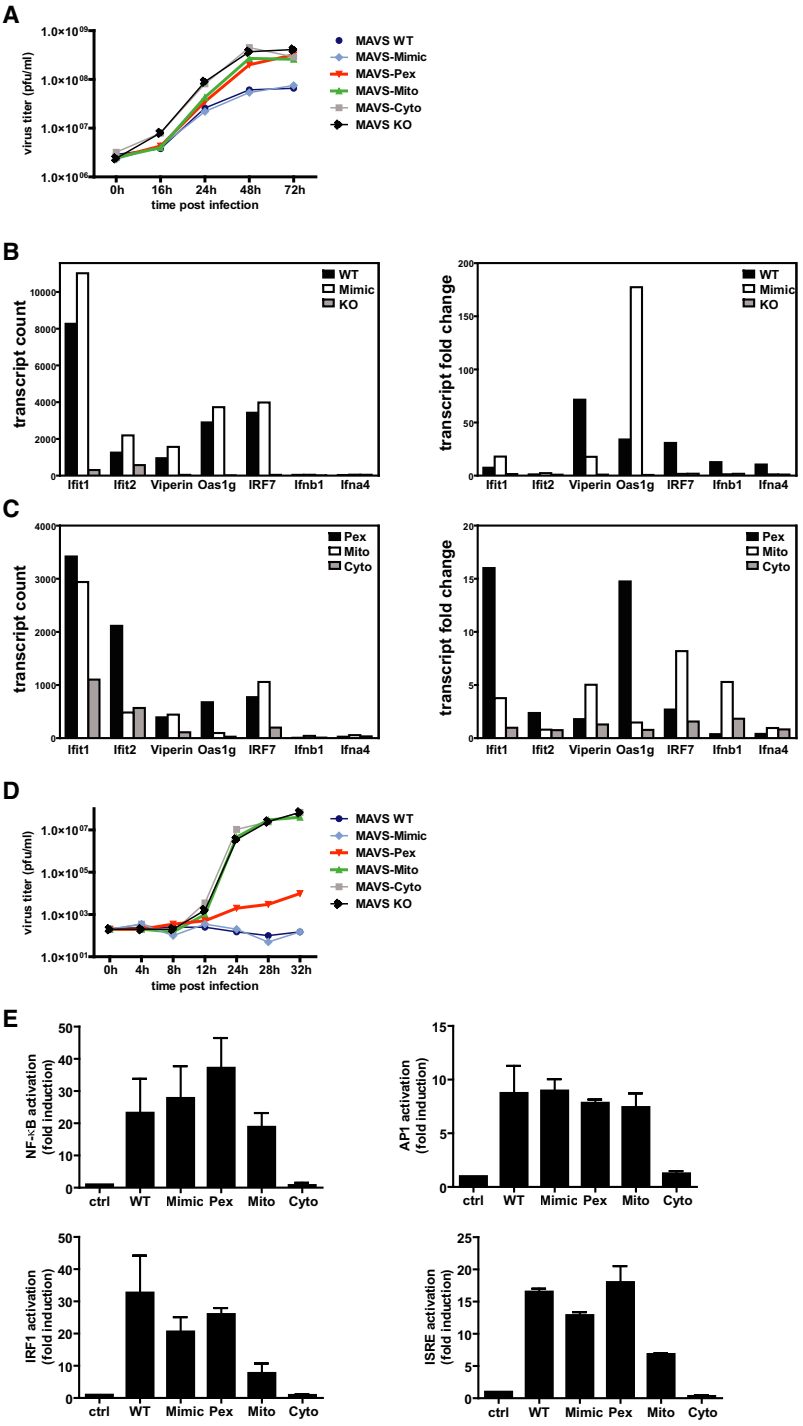

Figure 6. Peroxisomal MAVS Elicits a Functional Antiviral Response

(A) MAVS-expressing MEFs and MAVS-KO MEFs were infected with reovirus at an MOI of 3. At the indicated times, virus titers were determined by plaque assay.

(B) MAVS-WT, -Mimic-expressing cells and MAVS-KO MEFs were infected with VSV at an MOI of 3. After 8 hr, RNA was isolated and analyzed for ISG and type I IFN expression with nCounter.

(C) Same as (B) except MAVS-Pex, MAVS-Mito, and MAVS-Cyto MEFs were analyzed.

(D) MAVS-expressing MEFs and parental MAVS-KO cells were infected with VSV at an MOI of 0.01. At the indicated times, virus titers were determined by plaque assay.

(E) 293T cells were transiently transfected with an ISRE, IRF1, NF-κB, or AP1 luciferase reporters together with empty pMSCV vector (control) or MAVS (WT, Mimic, Pex, Mito, or Cyto). Results were normalized to Renilla luciferase activity and are shown as fold increase relative to cells transfected with empty vector. Error bars show standard deviation of triplicate transfections.

See also Figure S5.

induced by VSV in cells expressing MAVS-Mito (Figure 6C). MEFs derived from various IRF-KO mice were infected with VSV and assessed for their ability to induce ISGs. Whereas WT cells induced the expression of several ISGs (and no IFNs), cells lacking IRF1 or IRF3 were incapable of inducing ISG expression (Figures 7A and 7B). A few ISGs (e.g., OAS1g) also required another family member, IRF5. These data indicate that IRF1 and IRF3 are central regulators of IFN-independent ISG expression and may act downstream of peroxisomal MAVS.

Cell Type-Specific Actions of Peroxisomal and Mitochondrial MAVS

The prototypical innate-immune adaptor MyD88 regulates TLR signaling and induces different transcriptional responses in different cell types. Whether other adaptor proteins also display this diversity of responses is unclear. To address this for MAVS, we examined the function of peroxisomal and mitochondrial MAVS in macrophages. Each MAVS allele was expressed in immortalized bone marrow-derived macrophages isolated from MAVS-KO mice. The localization of each MAVS protein was similar to that observed in MEFs (compare Figures S2 and S5C). In response to reovirus infection, macrophages that contained mitochondrial MAVS (MAVS-WT or -Mito) induced transcripts encoding IFNs (Figure 7C) and ISGs (Figure S5D). MAVS-Cyto was unable to induce gene expression in response to reovirus infection. Unlike MEFs, reovirus-infected macrophages expressed inflammatory cytokines such as IL-1β (Figure 7D), IL-6, IL-12b, and TNFα (Figure S5D and data not shown). Another difference between MEFs and macrophages was that MAVS-Mito-expressing macrophages exhibited no kinetic delay in reovirus-induced gene expression. These results suggest that like the TLR adaptor MyD88, the function of MAVS is controlled in a cell type-specific way.

Peroxisomal MAVS induced the expression of some genes to the same levels observed with the WT allele, such as A20, IL-1β, Cox2, CXCL2 (MIP-2α), CCL4 (MIP-1β), and Fos (Figure 7D),

whereas others were induced more than 3-fold but still less than in WT cells, e.g., viperin, IFIT1, and IFIT2 (Figure S5D). Of note, peroxisomal MAVS was unable to induce the expression of any IFN gene in macrophages (Figure 7C). Thus, despite cell type-specific activities of MAVS, a fundamental feature of the RLR signaling network appears to be that peroxisomal MAVS functions to promote an IFN-independent means of gene expression.

DISCUSSION

The best-characterized sensors of cytosolic viruses are members of the RLR family, which enlist the adaptor protein MAVS to initiate antiviral signaling (Kawai and Akira, 2007). MAVS is one of a growing group of tail-anchored membrane proteins, which contain a C-terminal transmembrane domain (Gandre-Babbe and van der Bliek, 2008; Koch et al., 2005; Seth et al., 2005). This anchor was originally reported to promote MAVS recruitment to the mitochondrial outer membrane, providing a landmark of where RLR signaling can occur (Seth et al., 2005). This discovery established that cytosolic detection systems, like extracellular detection systems (e.g., TLRs), use membranes as scaffolds for signal transduction. In the TLR network, however, signaling occurs from a variety of different organelles, not just one (Barton and Kagan, 2009). We report here that in addition to mitochondria, the antiviral signaling protein MAVS is located on peroxisomes in several human and murine cell types.

The central finding of this study—that peroxisomes are a site of signal transduction—was established with a complementary set of assays that measured (1) messenger RNAs (mRNAs) encoding ISGs and IFNs, (2) protein levels of ISGs and IFNs, (3) the induction of a functional antiviral state in cells, and (4) infection-induced changes in peroxisome morphology. In each of these assays, we found that peroxisomes are a site of MAVS-dependent signaling. Moreover, we obtained these results by using several unrelated RNA viruses as physiological triggers of RLR signaling, which suggests that peroxisomal signaling is a fundamental component of the RLR network.

The RLR signaling network now joins the TLRs as pattern recognition systems that signal from multiple organelles. Both systems require that a transmembrane protein be positioned on specific organelles—the receptors themselves in the case of TLRs and the MAVS adaptor in the case of RLRs (Akira et al., 2006; Barton and Kagan, 2009). Interestingly, when considering these two networks, the function of diversifying signaling locale appears to be distinct. In the case of TLRs, differential receptor placement diversifies the types of pathogens that can be detected: TLRs found on endosomes recognize viruses, while TLRs found on the plasma membrane typically recognize bacteria. In contrast, differential MAVS placement does not diversify the types of viruses detected by RLRs, but diversifies the types of signaling pathways that are activated. In the case of reovirus and influenza virus infection of fibroblasts, peroxisomal MAVS triggers the rapid expression of ISGs, whereas mitochondrial MAVS triggers delayed ISG and IFN expression. This diversification is functionally important, as our data indicate that MAVS signaling must occur from both organelles to limit reovirus replication.

Our studies revealed another important similarity between the RLR and TLR networks, that of cell type-specific functions for adaptor proteins. In fibroblasts, MAVS functioned to induce expression of IFNs and ISGs, but not inflammatory cytokines. In contrast, IFNs, ISGs, and cytokines were all induced by MAVS signaling in macrophages. Thus, MAVS can be grouped with the TLR adaptor MyD88 as immune regulators that induce cell type-specific transcriptional responses. What is the benefit of cell type-specific actions of innate immune signaling pathways? One benefit may lie in the primary functions of the cells responding to a given virus. For example, macrophages are dedicated sentinels of the innate immune system. As such, within these cells, infection triggers MAVS-dependent inflammatory cytokine production and antiviral factors. Fibroblasts, in contrast, are tissue-resident cells that are primarily involved in organ homeostasis—a condition that is disrupted under inflammatory conditions. Thus, designing MAVS to induce antiviral factors but not inflammatory cytokines in fibroblasts may aid these cells in maintaining homeostasis under infectious conditions. We speculate that the diversification of adaptor functions in innate immunity may be a general mechanism to tailor signaling pathways to the needs of functionally diverse cell types.

Our finding that peroxisomal localization of MAVS is required for rapid but transient induction of antiviral ISGs whereas mitochondrial MAVS promotes ISG expression with delayed kinetics in fibroblasts is especially intriguing. The kinetic differences of ISG expression were explained by the observation that peroxisomal MAVS induced a cell-intrinsic means of ISG induction, which occurred in the absence of detectable IFN expression. Mitochondrial MAVS induced cell-intrinsic ISG expression as well, but maximal induction occurred through the actions of secreted IFNs. Our studies did not reveal an obvious difference in the downstream regulators activated by peroxisomal versus mitochondrial MAVS, but the studies performed in 293T cells suggest that the selective positioning of negative regulators (e.g., NLRX1) may contribute to organelle-specific responses. Future work will be required to address this point.

The functional importance of RLR signaling from peroxisomes was best revealed by experiments with VSV, which interferes with IFN expression and renders the mitochondrial pathway ineffective. As a result, even though MAVS is present on mitochondria and peroxisomes in WT cells, a functional antiviral response against VSV is only induced by the peroxisomal pathway. We also exploited VSV infection to dissect the peroxisomal signaling pathway using cells derived from genetically-deficient mice. While we found that IRF3 plays a role in ISG expression, this factor is also involved in the regulation of IFN expression (Sato et al., 2000) and may therefore be considered a more general regulator of antiviral gene expression. Indeed IRF3 is also involved in IFN expression induced by non-RLRs (Kawai and Akira, 2007). IRF1, on the other hand, is needed for expression of all ISGs that we examined in VSV-infected cells and is not required for IFN expression (Tamura et al., 2008). IRF1 may thus uniquely control IFN-independent signaling events that lead to ISG expression and antiviral immunity. Our experiments with VSV also revealed a probable benefit of utilizing both IFN-dependent and IFN- independent mechanisms of ISG induction: for pathogens that disrupt the

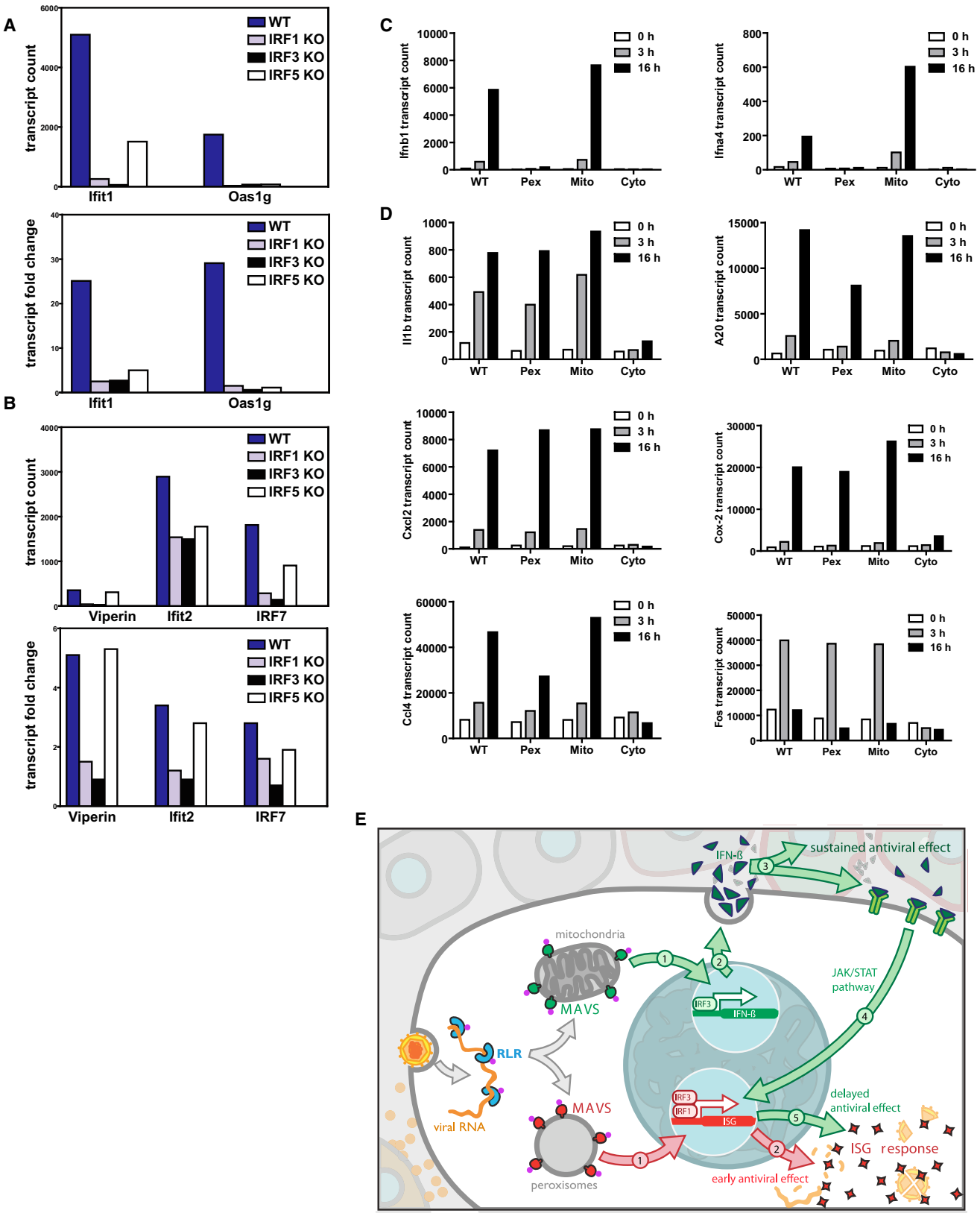
A
transcript count
WT
IRF1 KO
IRF3 KO
IRF5 KO
Ifit1
Oas1g
transcript fold change
B
Viperin
Ifit2
IRF7
C
Ifnb1 transcript count
Ifna4 transcript count
0 h
3 h
16 h
WT
Pex
Mito
Cyto
D
Il1b transcript count
A20 transcript count
Cxcl2 transcript count
Cox-2 transcript count
Ccl4 transcript count
Fos transcript count
E
IFN-ß
sustained antiviral effect
mitochondria
MAVS
RLR
viral RNA
JAK/STAT pathway
IRF3
IFN-ß
IRF1
ISG
delayed antiviral effect
ISG response
early antiviral effect
peroxisomes

expression of IFNs, the peroxisomal pathway retains the ability to induce ISGs and create a functional, albeit temporary, antiviral state.

In fibroblasts, the cooperative actions of MAVS on peroxisomes and mitochondria are needed for maximal antiviral immunity, and signaling from each organelle occurs independently of the other. As such, it appears that a simple mathematical equation can be proposed to explain antiviral signal transduction: RLR = Pex + Mito (Figure 7E). If either term in this equation is removed, then the RLR signaling network operates inefficiently, and antiviral immunity is compromised. We note however, that maximal ISG and IFN expression requires signaling from both organelles, which likely indicates that crosstalk exists to allow the two pathways to be properly integrated.

In closing, our studies establish a new function for peroxisomes, that of a subcellular compartment that promotes a rapid response to viral infection. We speculate that additional organelles may harbor pathogen detection systems, and our work provides a mandate to expand the search for these organelles.

EXPERIMENTAL PROCEDURES

Plasmids and Antibodies

pCMV2 Flag-IPS-1, pEF-HA-MAVS, pCDNA3-HA-NLRX1, and the myc-Mff plasmid were gifts from S. Akira, Z. Chen, J.Ting, and A. van der Bliek, respectively. The plasmids Dsred-PTS1, bicistronic Pex19 / EGFP-PTS1, Pex19, EGFP-Pex19, Pex13p-EGFP, and pCMV-TIRAP-flag have been described (Fransen et al., 2001; Horng et al., 2001; Vastiau et al., 2006). Pex19 was amplified from EGFP-Pex19 and inserted into the retroviral vector pMSCV IRES GFP. All MAVS constructs are based on the allele BC044952. The full-length (1–540) and a truncated (1–500) sequence were amplified from pEF-HA-MAVS by PCR. For chimeric MAVS alleles, the C-terminal 40 residues were replaced by the following sequences: PEX13 (NM_002618) residues 136–233, FIS1 (NM_016068) residues 127–152, and Omp25 (NM_022599) residues 109–145 by overlap extension PCR and cloned into pMSCV IRES GFP.

Anti-Pex19 and anti-Pex14, anti-viperin, and anti-myc 9E10 were gifts from M. Fransen, P. Cresswell, and S. Hansen, respectively. Anti-MAVS (Bethyl Laboratories), anti-mtHSP70 (ABR Affinity Reagents), anti-Flag M2 (Sigma), anti-Fis (Santa Cruz), anti-HA (Roche), and anti-β-actin (Sigma) were used according to the manufacturers' recommendations.

Cell Lines, Retroviral Gene Transfer, and Cell Fractionation

MEFs, Huh-7, 293T, Vero, and MDCK cells were cultured according to standard techniques. MAVS-KO MEFs, PEX19-deficient human skin fibroblasts, and L929 cells stably expressing an ISRE-luciferase reporter were provided by Z. Chen, R. Wanders, and B. Beutler, respectively. MEFs lacking IRF1, 3, and 5 were provided by K. Fitzgerald. MAVS and PEX19 alleles were introduced in MAVS-KO MEFs and Pex19-deficient human skin fibroblasts by retroviral gene transfer and then sorted for equal GFP fluorescence to normalize MAVS expression levels. Fractionations of HepG2 cells were performed as described (Fransen et al., 2004).

DNA Transfections and Immunofluorescence

MEFs and Huh-7 cells were transfected with Fugene-6 (Roche) for 24 hr at 37°C. Where indicated, cells were incubated with 250 nM MitoTracker Deep Red FM (Molecular Probes) for 30 min at 37°C prior to fixation. For NLRX1 visualization, Huh-7 cells expressing HA-NLRX1 were incubated with 160 nM MitoTracker for 20 min at 37°C and permeabilized with 0.1% saponin in 80 mM PIPES, 5 mM EGTA, and 1 mM $MgCl_2$ (pH 6.8) for 10 min at 25°C. Cells were fixed with 2% paraformaldehyde for 20 min at 25°C and permeabilized for 10 min with 0.1% Triton X-100. Samples were treated with block buffer (2% goat serum and 50 mM ammonium chloride in PBS) for 30 min, and the appropriate antibodies were diluted in block buffer. Antibody binding was detected using antibodies conjugated with Alexa fluor 488, 594, or 647 (Molecular Probes). Samples were imaged on a Nikon TE-2000 inverted microscope fitted with a video-rate confocal system consisting of a spinning disk confocal head (Yokogawa). Using a 100× oil immersion objective with a numerical aperture of 1.4, confocal images were collected as a 3D stack with a focal step size of 0.27 μm. Micrographs were processed with Adobe Photoshop.

Virus Stocks, Infections, and Plaque Assay

Reovirus Type 3 Dearing (Cashdollar lab clone) was propagated on L929 cells and plaque purified as described (Furlong et al., 1988). Cells were seeded 12–16 hr prior to infection on 6-well plates. On the day of infection, medium was replaced by addition of 2 ml fresh medium containing virions at a multiplicity of infection (MOI) of 100, unless stated otherwise. Where indicated, cells were preincubated with 20 μg/ml brefeldin A (Invitrogen) and infections were carried out in the presence of the drug. Type I IFN activity was blocked by addition of 250 neutralizing units/ml anti-IFNβ and 500 neutralizing units/ml anti-IFNα (PBL InterferonSource) antibodies at the time of infection. So that reovirus replication could be assessed, purified virions were diluted in 100 μl attachment buffer (phosphate-buffered saline with 2 mM $MgCl_2$) and incubated with cell monolayers for 1 hr at room temperature. After removal of unabsorbed virus by two washes with attachment buffer, cells were incubated for the indicated times. Next, cells were lysed by freeze/thaw and infectious titers were measured by serial dilution onto L929 cells as described (Middleton et al., 2007).

Influenza virus (A/Puerto Rico/8/34, H1N1) lacking the NS1 gene was propagated in Vero cells as described (García-Sastre et al., 1998) and titrated by plaque assay on MDCK cells. For infection, cell monolayers were incubated with ΔNS1 virus at a MOI of 5 for 1 hr at 37°C in Dulbecco's modified Eagle's medium supplemented with 0.3% bovine serum albumin, washed, and incubated with growth media.

VSV (Indiana) infections were performed as described (Cureton et al., 2009), and viral titer was determined by plaque assay on Vero cells.

Immunoblotting and Type I IFN Bioassay

Protein extracts were prepared by standard techniques, and 40 μg cell extract was separated by SDS-PAGE and analyzed by immunoblot. Type I IFN activity was measured as described (Jiang et al., 2005).

Gene Arrays and Bioinformatics

Cells were infected as described above, and RNA was purified with QIAShredder and the RNeasy Mini Kit (QIAGEN). Microarrays were performed by the Molecular Genetics Core Facility at Children's Hospital Boston supported by NIH-P50-NS40828 and NIH-P30-HD18655. Quantile normalization was used for signal extraction and normalization. Two criteria were applied to identify

Figure 7. Transcription Factors that Control Peroxisomal MAVS Signaling

(A and B) WT, IRF1, IRF3, and IRF5 KO MEFs were infected with VSV at an MOI of 3. After 8 hr, RNA was isolated and analyzed for ISG and type I IFN expression with nCounter.

(C and D) Immortalized MAVS-KO macrophages were retrovirally transduced with MAVS-WT, -Pex, -Mito, and-Cyto for 48 hr. The transduction efficiency of each cell population was determined to be 20%–30% as assessed by fluorescence microscopy. Cells were infected with reovirus and at the indicated times and were harvested, and RNA was analyzed for expression of type I IFN (C) and other inflammatory genes (D) with nCounter. See also Figure S5.

(E) Model of organelle specific MAVS signaling in fibroblasts. Peroxisomal MAVS is essential for rapid ISG expression independent of type I IFN, whereas mitochondrial MAVS induces ISGs with delayed kinetics and primarily dependent on type I IFN secretion. Therefore, peroxisomal MAVS mediates immediate and transient antiviral effects, while mitochondrial MAVS promotes a sustained response later during infection. See also Figure S5.

differentially regulated genes: (1) statistical significance of $p < 0.05$ and (2) fold change of greater than 2 (ratio > 2.0 or < 0.5). Four thousand eighty-nine genes passed both criteria for at least one of the assayed conditions. Samples are clustered based on the Pearson's correlation coefficient for the profile of those 4089 genes. The Pearson correlation, hierarchical clustering, and heat map were generated with the R functions "cor," "hclust," and "heatmap," respectively. Signal intensity that reflected mRNA expression was presented on heat maps or scatterplots on a log scale according to a color-coded intensity scale with R software (The R Project for Statistical Computing). Each data point in the scatterplots presented indicates a gene whose expression level exhibited a change >2-fold.

mRNA Detection and Analysis with nCounter

nCounter CodeSets were constructed to detect genes selected by the GeneSelector algorithm and additional controls as described. Two hundred and forty thousand cells were lysed in RLT buffer (QIAGEN) supplemented with β-mercaptoethanol. Five percent of the lysate was hybridized for 16 hr with the CodeSet and loaded onto the nCounter prep station, followed by quantification with the nCounter Digital Analyzer. To allow for side-by-side comparisons of nCounter experiments, we normalized the nCounter data in two steps. We first controlled for small variations in the efficiency of processing by normalizing measurements from all samples analyzed on a given run to the levels of chosen positive controls provided by the nCounter instrument. Second, we normalized the data obtained for each sample to the expression of nine control genes (Gapdh, Ik, Mea1, Ndufs5, Ndufa7, Rbm6, Shfm1, Tomm7, and Ywhaz). These genes were described to be unchanged in cells exposed to a variety of infectious conditions (Amit et al., 2009). For every sample, we computed the weighted average of the mRNA counts of the nine control transcripts and normalized the sample's values by multiplying each transcript count by the weighted average of the controls.

ACCESSION NUMBERS

The microarray data discussed in this publication are accessible through GEO Series accession number GSE21215 (http://www.ncbi.nlm.nih.gov/geo/query/acc.cgi?acc=GSE21215).

SUPPLEMENTAL INFORMATION

Supplemental Information includes five figures and can be found with this article online at doi:10.1016/j.cell.2010.04.018.

ACKNOWLEDGMENTS

We would like to thank B. Boush (FACS), J. Wagner (microscopy), and C. Brees (cell fractionation) for expert help. We would like to thank S. Brubaker, C. Glanemann, L.R. Marek, M. Schneider, and I. Zanoni for helpful discussions. This work has been supported by the following sources: Children's Hospital Boston Career Development Fellowship (J.K.), Austrian Science Fund (FWF; DK CCHD W1205) (E.D.), Fonds voor Wetenschappelijk Onderzoek—Vlaanderen (G.0754.09) and the Bijzonder Onderzoeksfonds of the K.U. Leuven (OT/09/045) (M.F.), the National Institutes of Health (AI059371 to S.P.W.); the Bill and Melinda Gates Foundation (S.B. and M.L.N., through a Vaccine Discovery Consortium grant to the International AIDS Vaccine Initiative), and the National Defense Science and Engineering Graduate Fellowship (A.S.Y.L.).

Received: November 18, 2009
Revised: February 16, 2010
Accepted: April 14, 2010
Published online: May 6, 2010

REFERENCES

Ablasser, A., Bauernfeind, F., Hartmann, G., Latz, E., Fitzgerald, K.A., and Hornung, V. (2009). RIG-I-dependent sensing of poly(dA:dT) through the induction of an RNA polymerase III-transcribed RNA intermediate. Nat. Immunol. *10*, 1065–1072.

Akira, S., Uematsu, S., and Takeuchi, O. (2006). Pathogen recognition and innate immunity. Cell *124*, 783–801.

Amit, I., Garber, M., Chevrier, N., Leite, A.P., Donner, Y., Eisenhaure, T., Guttman, M., Grenier, J.K., Li, W., Zuk, O., et al. (2009). Unbiased reconstruction of a mammalian transcriptional network mediating pathogen responses. Science *326*, 257–263.

Balachandran, S., Venkataraman, T., Fisher, P.B., and Barber, G.N. (2007). Fas-associated death domain-containing protein-mediated antiviral innate immune signaling involves the regulation of Irf7. J. Immunol. *178*, 2429–2439.

Barton, G.M., and Kagan, J.C. (2009). A cell biological view of Toll-like receptor function: regulation through compartmentalization. Nat. Rev. Immunol. *9*, 535–542.

Castanier, C., Garcin, D., Vazquez, A., and Arnoult, D. (2010). Mitochondrial dynamics regulate the RIG-I-like receptor antiviral pathway. EMBO Rep. *11*, 133–138.

Chin, K.C., and Cresswell, P. (2001). Viperin (cig5), an IFN-inducible antiviral protein directly induced by human cytomegalovirus. Proc. Natl. Acad. Sci. USA *98*, 15125–15130.

Chiu, Y.H., Macmillan, J.B., and Chen, Z.J. (2009). RNA polymerase III detects cytosolic DNA and induces type I interferons through the RIG-I pathway. Cell *138*, 576–591.

Collins, S.E., Noyce, R.S., and Mossman, K.L. (2004). Innate cellular response to virus particle entry requires IRF3 but not virus replication. J. Virol. *78*, 1706–1717.

Cureton, D.K., Massol, R.H., Saffarian, S., Kirchhausen, T.L., and Whelan, S.P. (2009). Vesicular stomatitis virus enters cells through vesicles incompletely coated with clathrin that depend upon actin for internalization. PLoS Pathog. *5*, e1000394.

Ferran, M.C., and Lucas-Lenard, J.M. (1997). The vesicular stomatitis virus matrix protein inhibits transcription from the human beta interferon promoter. J. Virol. *71*, 371–377.

Fitzgerald, K.A., Palsson-McDermott, E.M., Bowie, A.G., Jefferies, C.A., Mansell, A.S., Brady, G., Brint, E., Dunne, A., Gray, P., Harte, M.T., et al. (2001). Mal (MyD88-adapter-like) is required for Toll-like receptor-4 signal transduction. Nature *413*, 78–83.

Fransen, M., Wylin, T., Brees, C., Mannaerts, G.P., and Van Veldhoven, P.P. (2001). Human pex19p binds peroxisomal integral membrane proteins at regions distinct from their sorting sequences. Mol. Cell. Biol. *21*, 4413–4424.

Fransen, M., Vastiau, I., Brees, C., Brys, V., Mannaerts, G.P., and Van Veldhoven, P.P. (2004). Potential role for Pex19p in assembly of PTS-receptor docking complexes. J. Biol. Chem. *279*, 12615–12624.

Furlong, D.B., Nibert, M.L., and Fields, B.N. (1988). Sigma 1 protein of mammalian reoviruses extends from the surfaces of viral particles. J. Virol. *62*, 246–256.

Gandre-Babbe, S., and van der Bliek, A.M. (2008). The novel tail-anchored membrane protein Mff controls mitochondrial and peroxisomal fission in mammalian cells. Mol. Biol. Cell *19*, 2402–2412.

García-Sastre, A., Egorov, A., Matassov, D., Brandt, S., Levy, D.E., Durbin, J.E., Palese, P., and Muster, T. (1998). Influenza A virus lacking the NS1 gene replicates in interferon-deficient systems. Virology *252*, 324–330.

Geiss, G.K., Bumgarner, R.E., Birditt, B., Dahl, T., Dowidar, N., Dunaway, D.L., Fell, H.P., Ferree, S., George, R.D., Grogan, T., et al. (2008). Direct multiplexed measurement of gene expression with color-coded probe pairs. Nat. Biotechnol. *26*, 317–325.

Gitlin, L., Barchet, W., Gilfillan, S., Cella, M., Beutler, B., Flavell, R.A., Diamond, M.S., and Colonna, M. (2006). Essential role of mda-5 in type I IFN responses to polyriboinosinic:polyribocytidylic acid and encephalomyocarditis picornavirus. Proc. Natl. Acad. Sci. USA *103*, 8459–8464.

Hettema, E.H., and Motley, A.M. (2009). How peroxisomes multiply. J. Cell Sci. *122*, 2331–2336.

Horng, T., Barton, G.M., and Medzhitov, R. (2001). TIRAP: an adapter molecule in the Toll signaling pathway. Nat. Immunol. *2*, 835–841.

Ingelmo-Torres, M., González-Moreno, E., Kassan, A., Hanzal-Bayer, M., Tebar, F., Herms, A., Grewal, T., Hancock, J.F., Enrich, C., Bosch, M., et al. (2009). Hydrophobic and basic domains target proteins to lipid droplets. Traffic *10*, 1785–1801.

Jiang, Z., Georgel, P., Du, X., Shamel, L., Sovath, S., Mudd, S., Huber, M., Kalis, C., Keck, S., Galanos, C., et al. (2005). CD14 is required for MyD88-independent LPS signaling. Nat. Immunol. *6*, 565–570.

Kato, H., Takeuchi, O., Sato, S., Yoneyama, M., Yamamoto, M., Matsui, K., Uematsu, S., Jung, A., Kawai, T., Ishii, K.J., et al. (2006). Differential roles of MDA5 and RIG-I helicases in the recognition of RNA viruses. Nature *441*, 101–105.

Kato, H., Takeuchi, O., Mikamo-Satoh, E., Hirai, R., Kawai, T., Matsushita, K., Hiiragi, A., Dermody, T.S., Fujita, T., and Akira, S. (2008). Length-dependent recognition of double-stranded ribonucleic acids by retinoic acid-inducible gene-I and melanoma differentiation-associated gene 5. J. Exp. Med. *205*, 1601–1610.

Kawai, T., and Akira, S. (2007). Antiviral signaling through pattern recognition receptors. J. Biochem. *141*, 137–145.

Koch, A., Yoon, Y., Bonekamp, N.A., McNiven, M.A., and Schrader, M. (2005). A role for Fis1 in both mitochondrial and peroxisomal fission in mammalian cells. Mol. Biol. Cell *16*, 5077–5086.

Loo, Y.M., Fornek, J., Crochet, N., Bajwa, G., Perwitasari, O., Martinez-Sobrido, L., Akira, S., Gill, M.A., García-Sastre, A., Katze, M.G., and Gale, M., Jr. (2008). Distinct RIG-I and MDA5 signaling by RNA viruses in innate immunity. J. Virol. *82*, 335–345.

Matsuzono, Y., Kinoshita, N., Tamura, S., Shimozawa, N., Hamasaki, M., Ghaedi, K., Wanders, R.J., Suzuki, Y., Kondo, N., and Fujiki, Y. (1999). Human PEX19: cDNA cloning by functional complementation, mutation analysis in a patient with Zellweger syndrome, and potential role in peroxisomal membrane assembly. Proc. Natl. Acad. Sci. USA *96*, 2116–2121.

Middleton, J.K., Agosto, M.A., Severson, T.F., Yin, J., and Nibert, M.L. (2007). Thermostabilizing mutations in reovirus outer-capsid protein mu1 selected by heat inactivation of infectious subvirion particles. Virology *361*, 412–425.

Moore, C.B., Bergstralh, D.T., Duncan, J.A., Lei, Y., Morrison, T.E., Zimmermann, A.G., Accavitti-Loper, M.A., Madden, V.J., Sun, L., Ye, Z., et al. (2008). NLRX1 is a regulator of mitochondrial antiviral immunity. Nature *451*, 573–577.

Mossman, K.L., Macgregor, P.F., Rozmus, J.J., Goryachev, A.B., Edwards, A.M., and Smiley, J.R. (2001). Herpes simplex virus triggers and then disarms a host antiviral response. J. Virol. *75*, 750–758.

Nakhaei, P., Genin, P., Civas, A., and Hiscott, J. (2009). RIG-I-like receptors: sensing and responding to RNA virus infection. Semin. Immunol. *21*, 215–222.

Nemoto, Y., and De Camilli, P. (1999). Recruitment of an alternatively spliced form of synaptojanin 2 to mitochondria by the interaction with the PDZ domain of a mitochondrial outer membrane protein. EMBO J. *18*, 2991–3006.

Pichlmair, A., Schulz, O., Tan, C.P., Näslund, T.I., Liljeström, P., Weber, F., and Reis e Sousa, C. (2006). RIG-I-mediated antiviral responses to single-stranded RNA bearing 5′-phosphates. Science *314*, 997–1001.

Sacksteder, K.A., Jones, J.M., South, S.T., Li, X., Liu, Y., and Gould, S.J. (2000). PEX19 binds multiple peroxisomal membrane proteins, is predominantly cytoplasmic, and is required for peroxisome membrane synthesis. J. Cell Biol. *148*, 931–944.

Saha, S.K., Pietras, E.M., He, J.Q., Kang, J.R., Liu, S.Y., Oganesyan, G., Shahangian, A., Zarnegar, B., Shiba, T.L., Wang, Y., and Cheng, G. (2006). Regulation of antiviral responses by a direct and specific interaction between TRAF3 and Cardif. EMBO J. *25*, 3257–3263.

Sato, M., Suemori, H., Hata, N., Asagiri, M., Ogasawara, K., Nakao, K., Nakaya, T., Katsuki, M., Noguchi, S., Tanaka, N., and Taniguchi, T. (2000). Distinct and essential roles of transcription factors IRF-3 and IRF-7 in response to viruses for IFN-alpha/beta gene induction. Immunity *13*, 539–548.

Seth, R.B., Sun, L., Ea, C.K., and Chen, Z.J. (2005). Identification and characterization of MAVS, a mitochondrial antiviral signaling protein that activates NF-kappaB and IRF 3. Cell *122*, 669–682.

Severa, M., Coccia, E.M., and Fitzgerald, K.A. (2006). Toll-like receptor-dependent and -independent viperin gene expression and counter-regulation by PRDI-binding factor-1/BLIMP1. J. Biol. Chem. *281*, 26188–26195.

Tamura, T., Yanai, H., Savitsky, D., and Taniguchi, T. (2008). The IRF family transcription factors in immunity and oncogenesis. Annu. Rev. Immunol. *26*, 535–584.

Vastiau, I.M., Anthonio, E.A., Brams, M., Brees, C., Young, S.G., Van de Velde, S., Wanders, R.J., Mannaerts, G.P., Baes, M., Van Veldhoven, P.P., and Fransen, M. (2006). Farnesylation of Pex19p is not essential for peroxisome biogenesis in yeast and mammalian cells. Cell. Mol. Life Sci. *63*, 1686–1699.

Wanders, R.J. (2004). Peroxisomes, lipid metabolism, and peroxisomal disorders. Mol. Genet. Metab. *83*, 16–27.

Yasukawa, K., Oshiumi, H., Takeda, M., Ishihara, N., Yanagi, Y., Seya, T., Kawabata, S., and Koshiba, T. (2009). Mitofusin 2 inhibits mitochondrial antiviral signaling. Sci. Signal. *2*, ra47.

Yoneyama, M., Kikuchi, M., Natsukawa, T., Shinobu, N., Imaizumi, T., Miyagishi, M., Taira, K., Akira, S., and Fujita, T. (2004). The RNA helicase RIG-I has an essential function in double-stranded RNA-induced innate antiviral responses. Nat. Immunol. *5*, 730–737.

Yoshida, R., Takaesu, G., Yoshida, H., Okamoto, F., Yoshioka, T., Choi, Y., Akira, S., Kawai, T., Yoshimura, A., and Kobayashi, T. (2008). TRAF6 and MEKK1 play a pivotal role in the RIG-I-like helicase antiviral pathway. J. Biol. Chem. *283*, 36211–36220.

OPEN ACCESS Freely available online

PLoS PATHOGENS

The Length of Vesicular Stomatitis Virus Particles Dictates a Need for Actin Assembly during Clathrin-Dependent Endocytosis

David K. Cureton[1], Ramiro H. Massol[2], Sean P. J. Whelan[3]*, Tomas Kirchhausen[1]*

1 Department of Cell Biology, Harvard Medical School, and Immune Disease Institute at Children's Hospital, Boston, Massachusetts, United States of America, **2** The Division of Gastroenterology and Nutrition, Children's Hospital, Boston, Massachusetts, United States of America, **3** Department of Microbiology and Molecular Genetics, Harvard Medical School, Boston, Massachusetts, United States of America

Abstract

Microbial pathogens exploit the clathrin endocytic machinery to enter host cells. Vesicular stomatitis virus (VSV), an enveloped virus with bullet-shaped virions that measure 70×200 nm, enters cells by clathrin-dependent endocytosis. We showed previously that VSV particles exceed the capacity of typical clathrin-coated vesicles and instead enter through endocytic carriers that acquire a partial clathrin coat and require local actin filament assembly to complete vesicle budding and internalization. To understand why the actin system is required for VSV uptake, we compared the internalization mechanisms of VSV and its shorter (75 nm long) defective interfering particle, DI-T. By imaging the uptake of individual particles into live cells, we found that, as with parental virions, DI-T enters *via* the clathrin endocytic pathway. Unlike VSV, DI-T internalization occurs through complete clathrin-coated vesicles and does not require actin polymerization. Since VSV and DI-T particles display similar surface densities of the same attachment glycoprotein, we conclude that the physical properties of the particle dictate whether a virus-containing clathrin pit engages the actin system. We suggest that the elongated shape of a VSV particle prevents full enclosure by the clathrin coat and that stalling of coat assembly triggers recruitment of the actin machinery to finish the internalization process. Since some enveloped viruses have pleomorphic particle shapes and sizes, our work suggests that they may use altered modes of endocytic uptake. More generally, our findings show the importance of cargo geometry for specifying cellular entry modes, even when the receptor recognition properties of a ligand are maintained.

Citation: Cureton DK, Massol RH, Whelan SPJ, Kirchhausen T (2010) The Length of Vesicular Stomatitis Virus Particles Dictates a Need for Actin Assembly during Clathrin-Dependent Endocytosis. PLoS Pathog 6(9): e1001127. doi:10.1371/journal.ppat.1001127

Editor: John A. T. Young, The Salk Institute for Biological Studies, United States of America

Received June 3, 2010; **Accepted** September 1, 2010; **Published** September 30, 2010

Funding: This work was supported by NIH (http://www.nih.gov/) grants U54 AI057159 (New England Regional Center of Excellence in Biodefense and Emerging Infectious Disease (NERCE BEID)) to TK and AI081842 to SPJW. The funders had no role in study design, data collection and analysis, decision to publish, or preparation of the manuscript.

Competing Interests: The authors have declared that no competing interests exist.

* E-mail: kirchhausen@crystal.harvard.edu (TK); swhelan@hms.harvard.edu (SPJW)

Introduction

Eukaryotic cells internalize constituents of the plasma membrane and extracellular cargos by entrapping them in membrane-bound carriers. The most prominent and well-characterized endocytic carriers are clathrin-coated vesicles (reviewed in [1–3]). Coated vesicles transport lipids, proteins, and other essential macromolecules from the cell surface to endosomal organelles. Extensive biochemical and cell biological research supports the following model for conventional coated vesicle formation in higher eukaryotes. The AP-2 clathrin adaptor complex recruits clathrin to the cytosolic leaflet of the plasma membrane and sequesters cargos at the endocytic site [4,5]. The continued assembly of clathrin into a lattice-like configuration helps deform the underlying membrane and ultimately creates an invagination, or 'pit' [2]. Recruitment of the GTPase, dynamin, then facilitates scission of the coated pit from the plasma membrane [6], and clathrin is rapidly removed from the cargo-loaded vesicle by the combined action of the heat shock cognate protein 70 (Hsc70) and its co-chaperone auxilin [7,8]. The entire process is typically complete within 30–60 s [9,10].

Coated pits incorporate and internalize soluble cargos of various sizes, such as transferrin (5 nm) [9,11] and low density lipoproteins (25 nm) [9,12]. Many viruses and intracellular bacteria are also internalized by the clathrin machinery [9,13–16]. We previously evaluated how cells internalize the 70×200 nm bullet-shaped vesicular stomatitis virus (VSV). We found that VSV internalization occurs through elongated, partially clathrin-coated structures that have longer lifetimes (~2 min.) than typical endocytic clathrin-coated vesicles and require local actin polymerization for uptake [15]. During VSV internalization, the clathrin coat first assembles as a partially closed dome at one end of the virion [15,17], and growth of the coat stalls when it encounters the long particle axis. Actin assembly then drives one or more late stage(s) of the internalization process, as recruitment of the actin machinery peaks during completion of clathrin assembly, and pharmacological inhibition of actin polymerization blocks VSV internalization without interfering with clathrin coat assembly [15]. Relatively small, spherical viruses like dengue virus (50 nm) [13] and some influenza A viruses (X-31 strain, ~120 nm) [14,18] also enter using a clathrin-dependent route, but it is unclear whether actin function is required for their uptake. Our observations with VSV led us to

Author Summary

We present a detailed comparison between the clathrin-dependent entry mechanisms of a parental virus (VSV) and its smaller defective interfering particle (DI-T). We used the difference in virion length to probe why actin assembly is required for the uptake of full-length VSV particles by nonpolarized mammalian cells. By imaging the entry of single particles in an unbiased manner, we resolved differences in the maturation kinetics, clathrin content, and actin dependency of clathrin endocytic structures internalizing VSV or DI-T virions. Our principal finding is that, unlike VSV uptake, DI-T internalization does not induce or require robust actin polymerization. We have also established, for the first time, that the geometry of an endocytic cargo can alter the mechanism of clathrin uptake. We propose that VSV-containing clathrin structures display characteristics of 'frustrated' endocytic intermediates that cells resolve by using the force of actin assembly to deform the plasma membrane into a complete endocytic vesicle.

hypothesize that the physical dimensions of the virion block the ongoing polymerization of clathrin during its uptake, and that the stalled structure recruits regulators of actin assembly whose activity is required to complete the internalization process.

Defective interfering (DI) particles arise spontaneously during virus replication. Such particles depend upon coinfecting helper virus to support their replication but contain all the essential *cis*-acting regulatory elements for genome replication and assembly. One such well- characterized DI particle of VSV is termed DI-T, which lacks 82% of the viral genome [19,20]. Since the length of a VSV particle is dictated by the genome size [21], DI-T particles are 75 nm long and appear as truncated bullets by electron microscopy [22]. DI-T particles contain normal proportions of the viral structural proteins [23], including the viral surface glycoprotein (G), which mediates VSV attachment and entry into host cells.

Here we took advantage of significant differences in the physical dimensions of VSV and DI-T to investigate how the geometry of a viral cargo influences the actin-dependency of clathrin internalization. Using live cell fluorescence microscopic imaging, we compared the uptake mechanisms of VSV and DI-T at the single particle level. We report that in contrast to the clathrin- and actin-dependent uptake of VSV, the shorter DI-T particles enter cells through fully coated clathrin carriers that do not require actin dynamics for vesicle budding. These observations highlight the plasticity of the clathrin endocytic system, where clathrin coats serve as a scaffold to direct actin assembly when the clathrin machinery alone is not sufficient to mediate internalization.

Results

Biological properties of DI-T particles

To generate a clonal population of VSV DI-T particles, we recovered DI-T from cDNA (Figure 1A) [24] and amplified the particles by co-infection of cells with VSV [25]. We separated DI-T particles from VSV by rate zonal centrifugation in a sucrose density gradient. Electron microscopic analysis (Figure 1B, C) confirmed that VSV virions measure 70+/−8 nm by 204+/−14 nm (n = 114) [21], while the shorter DI-T particles have a length of 76+/−8 nm (n = 81) [22]. DI-T particles, like VSV, are covered with spike-like projections that correspond to homotrimers of G protein (Figure 1B), and SDS-PAGE analysis of purified particles confirmed that VSV and DI-T particles contain similar ratios of G protein to core virion components (Figure 1D) [23]. The purified stocks of DI-T lacked full-length virions (Figure 1B), with only a single VSV virion observed amongst more than 3,000 DI-T particles. Limited dilutions of the purified DI-T stock contained $\sim 1 \times 10^6$ plaque forming units of virus per microgram of total viral protein, or 10^{-5} times fewer infectious particles than for an equivalent protein quantity of VSV particles (not shown). Thus, we have successfully purified relatively homogeneous populations of VSV and DI-T particles, which differ only in their physical dimensions.

DI-T particles enter cells by clathrin-dependent endocytosis

To visualize VSV and DI-T by fluorescence microscopy, we covalently labeled the G proteins with spectrally separable fluorescent dye molecules (Alexa Fluor 568 and 647, respectively) using conditions that do not reduce viral infectivity [15]. Spinning disk confocal images of labeled particles adsorbed onto glass coverslips showed diffraction-limited objects with single-peaked distributions of fluorescence intensity values (Figure 1E), indicating that the DI-T and VSV populations primarily consist of individual particles [15]. We tracked the entry of DI-T particles into BSC1 cells stably expressing an eGFP-tagged σ2 subunit of the AP-2 adaptor complex (σ2-eGFP), which incorporates into all clathrin-coated structures that form on the plasma membrane [9,15,26]. Single DI-T particles readily attached to cells and progressed through the following set of defined events (see Figures 2A, B; Video S1 for examples): (1) membrane-bound DI-T particles diffused slowly ($D = 5 \times 10^{-11}$–5×10^{-12} cm^2 s^{-1}) and with the random directionality characteristic of Brownian motion; (2) shortly after DI-T attachment, a dim spot of AP-2 signal arose and remained colocalized with the particle, signifying incorporation of DI-T into an assembling clathrin-coated pit; (3) the AP-2 signal steadily increased over time until it peaked as coat assembly completed, and the DI-T particle then underwent an abrupt movement into the cell, after which the AP-2 signal disappeared due to clathrin uncoating. This sequence of events is identical to what we previously observed for VSV entering cells by clathrin-dependent endocytosis [15]. Moreover, the efficiency of DI-T uptake *via* the clathrin pathway is similar to that of the full-length VSV particles, as 89% (55/62) of DI-T particles that attached to 3 individual cells during imaging entered by clathrin-dependent endocytosis. These data show that DI-T efficiently enters cells through the clathrin pathway and validate the use of DI-T and VSV as comparative endocytic cargos.

Clathrin structures capture VSV and DI-T particles with similar kinetics

To directly compare how DI-T and VSV particles engage the clathrin machinery, we simultaneously inoculated BSC1 cells with the two spectrally distinct particle forms and then analyzed their mode of incorporation into AP-2 containing clathrin structures on a single cell basis (Figure 2C). For each complete virus uptake event, we quantified the kinetics of particle capture by measuring the elapsed time between virion attachment and the appearance of an AP-2 signal that colocalized with the bound particle. The capture time for DI-T particles was 110+/−80 s (n = 121), which is statistically indistinguishable (Student's *t*-test, p = 0.2) to that measured for VSV (130+/−125 s (n = 87)) and agrees well with our prior measurements (Figure 2D) [15]. The AP-2 structures that captured DI-T or VSV initiated within a ~250 nm zone (the resolution limit of the optical system) of the attached particle. We therefore conclude that DI-T and VSV particles engage the clathrin system in an indistinguishable manner, which likely reflects a shared mechanism triggered by the same viral glycoprotein-receptor interactions.

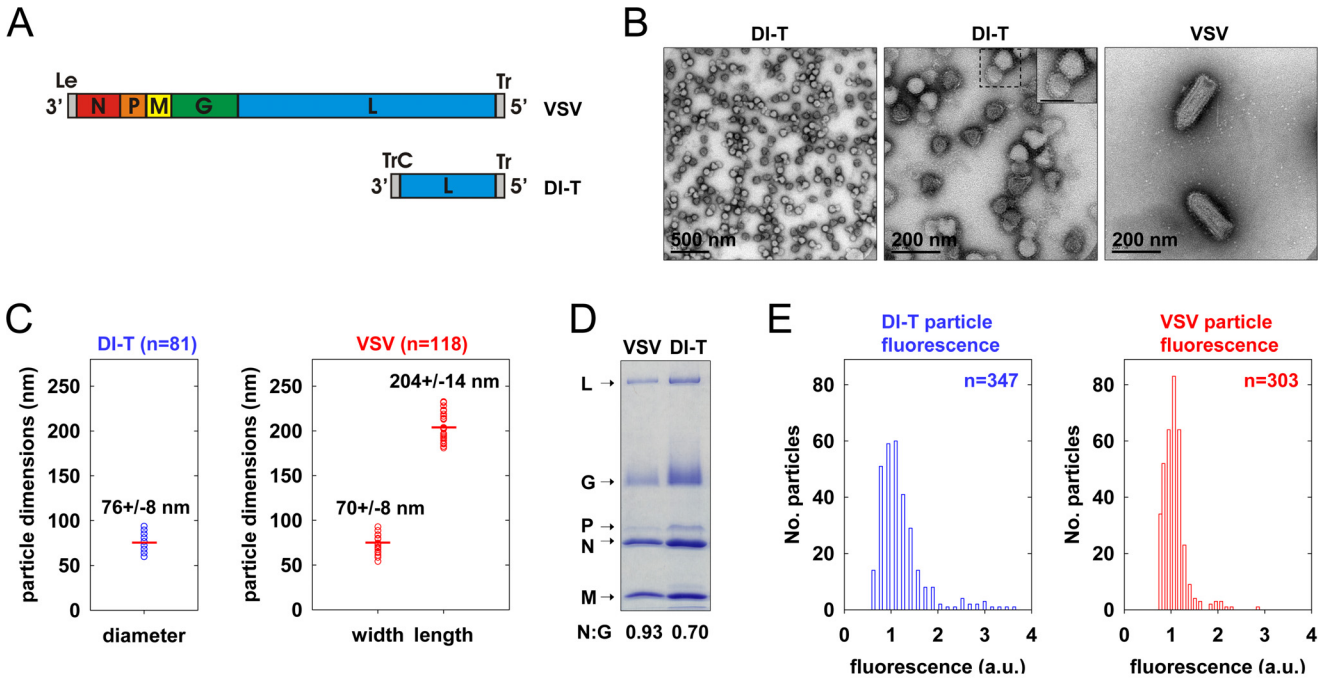

Figure 1. Biological properties of DI-T particles. (A) Structure of VSV and DI-T genomic RNAs. The single-stranded negative-sense RNA genomes are shown in a 3′-5′ orientation. The five viral genes are colored as follows: red nucleocapsid (N) protein gene; orange, phosphoprotein (P) gene; yellow, matrix (M) protein gene; green, glycoprotein (G) gene; blue, large (L) polymerase protein gene. The noncoding genomic terminal leader (Le) and trailer (Tr) regions, which serve as promoters for RNA synthesis and genomic RNA encapsidation, are shown in gray. The DI-T genome comprises 2,208 nts. The 5′ terminal 2,163 nts derive from the 5′ terminus of the parental VSV genome (11,161 nts), and the 3′terminus contains a 45 nt inverted complement of the wild-type Tr (TrC). (B) Electron micrographs of purified VSV and DI-T particles negatively stained with PTA. Middle panel, inset shows an expanded view of virions from the boxed region to facilitate visualization of the viral glycoprotein spikes. Inset scale bar, 100 nm. (C) Virion geometry. The dimensions of individual DI-T (blue) and VSV (red) particles measured from electron micrographs of negatively stained particles. Each open circle represents the measurement for a single particle. Horizontal red lines denote the mean value of each population, and the numerical means (+/− SD) are provided above each plot. (D) Protein composition of purified VSV and DI-T particles. Viral proteins (L, G, P, N, and M) were separated by SDS-PAGE and visualized with Coomassie blue staining. The ratio of N protein to G protein was quantified using ImageJ and is displayed below the gel as a comparative measure of average virion surface glycoprotein density in each particle population. (E) Fluorescence intensity of virus particles labeled with Alexa Fluor dye molecules. Purified DI-T or VSV particles were labeled with Alexa Fluor 647 or 568 and imaged on separate glass coverslips using a spinning disk confocal microscope. The fluorescence intensity of individual spots in a single field of view was quantified, and the distribution of intensity values (in arbitrary units, a.u.) for DI-T (blue) and VSV (red) particles is shown.
doi:10.1371/journal.ppat.1001127.g001

Cells internalize DI-T particles using conventional clathrin-coated vesicles

To investigate the characteristics of the clathrin coat responsible for DI-T internalization, we imaged the uptake of both particle forms by the same BSC1 cell. We found that DI-T particles are internalized through AP-2 containing structures significantly faster than full-length virions (Figure 3A, B; Video S2). Quantitative analysis of data compiled from 4 cells showed that pits incorporating DI-T (n = 36) form in 43+/−14 s, which is similar to the assembly kinetics of pits that lack virus particles (n = 212, 35+/−10 s) (Figure 3C, Table 1). As expected, AP-2 structures that capture VSV (n = 29) require longer (75+/−22 s) to complete (Figure 3C, Table 1). A similar analysis conducted in cells transiently expressing eGFP-tagged clathrin light chain A1 (eGFP-LCa) yielded analogous results (Figure 3D, E, Table 1, Videos S3, S4). The interaction of full-length VSV with a cell had no impact on the uptake kinetics of DI-T into the same cell (Table 1).

The different kinetics of DI-T versus VSV internalization suggests that DI-T enters cells through conventional fully coated clathrin structures and not the partially coated vesicles responsible for VSV uptake. To further investigate this possibility, we measured the maximum fluorescent signal of eGFP-tagged AP-2 or clathrin molecules, as this peak signal is known to be proportional to the overall size of a clathrin coat [9,15,26]. We compared this value for structures that contained DI-T with those that contained VSV or lacked either particle. Similar quantities of coat components were present in structures associated with DI-T to those lacking viral particles (Figure 3C, E, Table 1). As expected, VSV-containing structures accumulate more AP-2 and LCa molecules than structures lacking virus (Figure 3C, E, Table 1). Taken together, the above experiments suggest that DI-T enters cells through pits that acquire a full clathrin coat. Consistent with this, electron micrographs of DI-T particles captured during cell entry show particles present in circular pits entirely surrounded by a clathrin coat (Figure 4A). This is in marked contrast to the partial clathrin coat found at one end of the endocytic carriers that internalize VSV (Figure 4B) [15].

Clathrin structures containing VSV recruit more cortactin that pits that internalize DI-T

During the final phase of coat assembly, endocytic clathrin structures associated with VSV show a strong recruitment of cortactin, an F-actin and dynamin binding protein that activates Arp2/3-mediated assembly of branched actin filaments [15,27,28]. To determine whether DI-T uptake is associated with an acute recruitment of cortactin, we monitored internalization

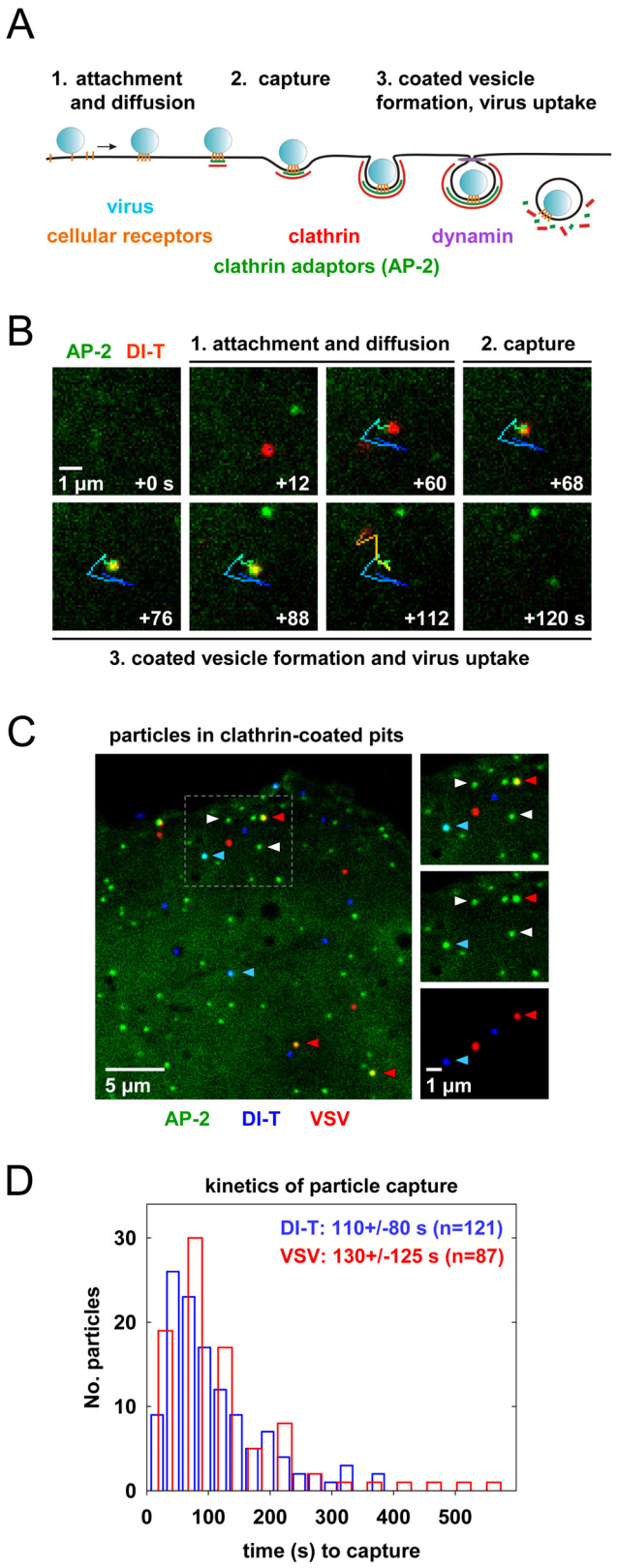

Figure 2. Clathrin structures capture VSV and DI-T particles with similar kinetics. (A) Schematic of clathrin-dependent virus internalization. 1. A particle (blue) attaches to receptor moieties (orange) on the cell surface (black horizontal line), and the virus-receptor complex diffuses in the plane of the membrane. 2. The virus particle is captured by the clathrin endocytic machinery (AP-2, green; clathrin, red) after diffusion into an existing clathrin structure (e.g. Dengue virus) or entrapment within a clathrin structure that initiates in close proximity to the virion (e.g. VSV and influenza A virus). 3. Clathrin assembly completes, and the virus-containing pit is severed from the cell surface in a dynamin-dependent process. Internalization of VSV also requires local actin assembly. Clathrin is rapidly removed from the nascent vesicle, and the vesicle is actively transported further into cell. (B) Example of a complete DI-T internalization event. A single DI-T particle (red) attaches to a BSC1 cell expressing σ2-eGFP (green) and diffuses on the cell surface. A dim spot of AP-2 appears beneath the virion, signifying capture of the particle. The AP-2 fluorescence intensity increases as the clathrin coat assembles, and the virus disappears into the cell shortly after the AP-2 signal reaches a maximum (Video S1). Numbered stages correspond to the events described in A. The path of particle motion is depicted as a linear, color-coded trace that progresses with time from blue to red. (C) VSV and DI-T particle capture by clathrin structures in the same cell. BSC1 cells stably expressing σ2-eGFP (green) were inoculated with Alexa Fluor 647-labeled DI-T (blue, blue arrowheads) and Alexa Fluor 568-labeled VSV (red, red arrowheads). Time-lapse images were acquired at 4 s intervals using a spinning disk confocal microscope. Left, snapshot of a cell depicting coated pits lacking (white arrowheads) or containing (blue/red arrowheads) virus particles. Right, expanded split-channel views of the region within the dashed box at left. (D) Kinetics of virus capture. BSC1 cells stably expressing σ2-eGFP (7 cells) or eGFP-LCa (12 cells) were inoculated with VSV and DI-T particles. Images were acquired at 3-4 s intervals as in C, and the time interval between virus attachment and detection of AP-2 or LCa beneath a virion was quantified for productive internalization events. The distribution of capture times is shown for DI-T (blue) and VSV (red) particles, and the mean time to capture (+/− SD) for each particle population is provided at right. The kinetics of VSV and DI-T capture are not significantly different (Student's *t*-test p value = 0.2).
doi:10.1371/journal.ppat.1001127.g002

into BSC1 cells transiently co-expressing monomeric Cherry-LCa (mCherry-LCa) and low levels of cortactin-eGFP. As previously shown [15,26,29], conventional clathrin-coated pits exhibit minimal cortactin recruitment that typically peaks just before completion of clathrin assembly (Figure 5A, Video S5). Cortactin recruitment is similarly sparse during the uptake of DI-T particles (Figure 5B, Video S6). In marked contrast, and as expected [15], large bursts of cortactin accompany the internalization of VSV (Figure 5C, Video S7). Quantitative analysis revealed that the peak fluorescence intensity of cortactin detected in the late phase of VSV uptake averaged 3-fold higher than the signal associated with pits containing DI-T or pits that did not capture a virus particle (Figure 5D, Table 1). These data suggest that while formation of short-branched actin filaments is required during the late stages of clathrin-mediated VSV entry, this need is obviated during clathrin-dependent DI-T entry.

Actin polymerization is not required for DI-T internalization

To directly test whether actin assembly is required for DI-T entry, we treated BSC1 cells with latrunculin B (latB), a chemical inhibitor of actin filament assembly [30], and tracked the endocytic fate of DI-T and VSV in the same cells. Treatment of cells with 6.3 μM latB did not change the efficiency of DI-T entry (Figure 6A–C, Video S8), but it reduced the internalization of VSV by >75% (Figure 6A–C). As expected [15], latB treatment did not affect the capture efficiency of either particle type by clathrin (Figure 6C). The lifetimes and AP-2 content of pits lacking particles or containing DI-T was similarly unaffected by latB (Figure 6D). We conclude that the shorter DI-T particles bypass the actin requirement displayed by the larger VSV for efficient clathrin-based uptake.

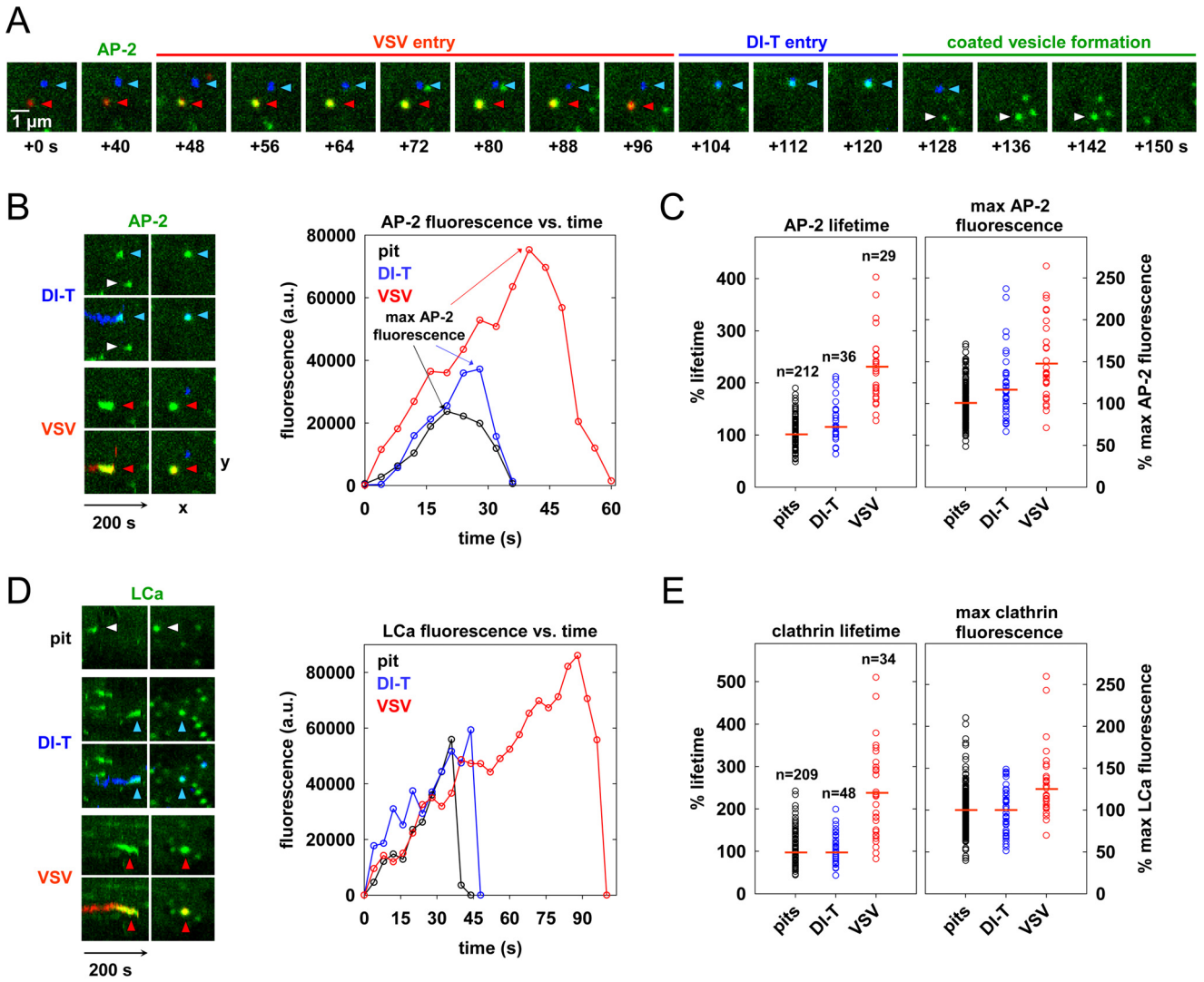

Figure 3. Cells internalize DI-T particles using conventional clathrin-coated vesicles. (A) Internalization of VSV and DI-T by the same cell. BSC1 cells stably expressing σ2-eGFP (green) were inoculated with VSV (red) and DI-T (blue) particles, and confocal images were captured at 4 s intervals. The images show the sequential internalization of single VSV (red, red arrowheads) and DI-T (blue, blue arrowheads) particles, followed by the formation of a canonical coated vesicle (white arrowhead) within a 3.5×3.5 µm^2 area of the plasma membrane (Video S2). The first acquired frame of the time-lapse series is designated +0 s, and the capture time of the subsequent images is shown. (B) AP-2 recruitment during the uptake events shown in A. Left, image quadrants depicting AP-2 accumulation over time (left panels) and at the time of maximum AP-2 signal during each event (right panels). Upper panels in each quadrant show the AP-2 channel alone, and the lower panels show overlays of the virus and AP-2 channels. The highlighted pit from A. is indicated with a white arrowhead, and virus particles are colored as in A. Right, fluorescence intensity (in arbitrary units, a.u.) of AP-2 over time for the events shown at left and in A. The time of AP-2 detection above the local background was set to t = 0 s for each event. (C) Kinetics and AP-2 content of endocytic structures. The plots show the relative lifetime (left) and maximum fluorescence intensity (right) of AP-2 during the uptake of coated pits lacking virus (pits, black) or structures that internalized DI-T (blue) or VSV (red) particles (from 4 cells). Values are expressed as percentages to facilitate comparison of viral and nonviral uptake events across multiple cells. Approximately 50 pits lacking virus were analyzed in each cell, and the mean of the measured values was calculated for each parameter. The values for each nonviral and viral uptake event were divided by the mean for pits lacking virus in the same cell, and the resulting values were multiplied by 100. Each open circle represents a single uptake event, and horizontal red lines demark the mean of the compiled population. The number of events is provided above each plot. Numerical values and statistical analyses are provided in Table 1. (D) Clathrin recruitment during virus entry. Left, kymograph views of internalization events from a single BSC1 cell transiently expressing eGFP-LCa (Videos S3, S4). Images were captured as in A. and displayed as described in B. Right, fluorescence intensity of eGFP-LCa over time for the events shown at left. (E) Kinetics and clathrin content of endocytic structures. The plots show the relative lifetime (left) and maximum fluorescence intensity (right) of clathrin during the uptake of coated pits lacking virus (pits, black) or structures that internalized DI-T (blue) or VSV (red) particles (from 3 cells). Data were calculated and plotted as described in C. Numerical values and statistical analyses are provided in Table 1.

doi:10.1371/journal.ppat.1001127.g003

Discussion

The major conclusion of our study is that the physical properties of a virus particle dictate the need for engagement of the actin system during its clathrin-dependent uptake into cells. We formulate this conclusion based on tracking the clathrin-dependent internalization of VSV and its shorter DI-T particle into live cells. Internalization of VSV is accompanied by the recruitment of

Table 1. Summary of kinetic and fluorescence intensity data.

Particle(s)	Fluorescent protein(s)	Treatment	# Expts /# Cells	Events analyzed	# Events	Lifetime	% Lifetime	% Max fluorescence
DI-T	σ2		1/3	DI-T	62	47+/−13 s	ND	ND
DI-T+VSV	σ2		1/4	pits	212	35+/−10 s	100+/−24	100+/−23
				DI-T	36	43+/−14 s	128+/−37**	119+/−38**
				VSV	29	75+/−22 s	224+/−68**	148+/−48**
	LCa		1/3	pits	209	44+/−19 s	100+/−34	100+/−26
				DI-T	48	44+/−14 s	100+/−30	99+/−26
				VSV	34	89+/−36 s	222+/−104**	130+/−38**
DI-T+VSV	σ2	+latB	2/4	pits	193	47+/−14 s	100+/−27	100+/−27
		+latB		DI-T	46	54+/−21 s	118+/−46*	133+/−42**
		+latB		VSV entry	20	141+/−104 s	298+/−198**	207+/−59**
		+latB		trapped VSV	31	615+/−216 s	1283+/−430**	192+/−73**
DI-T	LCa + cortactin		1/3	pits	155	51+/−19 s	100+/−34	100+/−50
				DI-T	30	65+/−28 s	129+/−63*	130+/−63*
			1/3	pits	220	52+/−24 s	100+/−36	100+/−66
VSV	LCa + cortactin			VSV	21	166+/−63 s	335+/−105**	300+/−164**

Kinetic and fluorescence values are provided as the mean +/− SD for all events in a given context. The number of experiments and cells analyzed is indicated. The absolute lifetimes are expressed in seconds (s). The % lifetime and % maximum fluorescence intensity values were calculated as described in the legend of Figure 3C. The % maximum fluorescence intensity of cortactin is provided for events analyzed in cells co-expressing mCherry-LCa and cortactin-eGFP. A two-tailed Student's *t*-test was used to determine whether data from 2 categories differ in a statistically significantly manner.

(*) denotes a statistical difference with a p-value <0.005 and >0.00005 when comparing data in a given category to data for pits lacking virus in the same category. (**) similarly denotes a p-value <0.00005. All values for VSV are significantly different ($p<0.005$ for % max AP-2 fluorescence; $p<0.00005$ for all other categories) from those measured for DI-T particles in the same context. ND, not determined.

doi:10.1371/journal.ppat.1001127.t001

cortactin at a late step of the endocytic process, and chemical inhibition of actin polymerization blocks virus uptake (this study and [15]). By contrast, internalization of the shorter DI-T particles is insensitive to chemical inhibition of actin polymerization and is not accompanied by the same spike of cortactin recruitment observed for the full-length VSV particles. VSV and DI-T particles differ in their length and not the density of the glycoprotein spike that dictates their entry. We suggest that the shape of the full-length VSV particles presents a physical barrier that frustrates completion of the clathrin-coated pit. The stalled clathrin structure then recruits the actin machinery required to finalize internalization. The shorter DI-T particles no longer provide such a physical barrier during engulfment, which results in their actin-independent internalization through coated vesicles that acquire a full complement of clathrin.

The importance of particle length for the clathrin-dependent uptake of VSV

Receptor-dependent signaling events lead to actin filament assembly during the clathrin-independent uptake of other viruses, including poliovirus and coxsackie B virus [31,32]. Here we show that the initial interactions of DI-T with the cell are indistinguishable to those of VSV, as both particle types diffuse slowly on the cell surface and are captured by coated pits with similar kinetics (Figure 2). Such similar behavior suggests that DI-T and VSV engage an as yet unknown viral receptor in an analogous manner. Since initial receptor interactions appear indistinguishable, it seems remote that VSV G-receptor interactions induce a signaling cascade that leads to actin polymerization at sites of VSV but not DI-T uptake. We therefore conclude that the glycoprotein is not the primary trigger of actin assembly during clathrin-dependent VSV internalization.

We previously showed that endocytic structures containing VSV do not acquire a full clathrin coat [15], which agreed with earlier electron micrographs depicting virus particles in tubular invaginations with clathrin at the cytosolic tip [17]. The morphology of those structures suggests that cells initially capture one tip of the virus particle, and clathrin assembly stalls when the constricting coat encounters the long axis of the virion (Figure 7). Here we found that DI-T particles do not alter the process of clathrin-coated vesicle formation (Figures 3, 4). This finding implies that clathrin can fully enclose cargos displaying VSV G provided that the particle shape does not physically prohibit clathrin assembly or closure of the plasma membrane (Figure 7). Consequently, the physical properties of the VSV particle captured by a clathrin-coated pit are what dictate the altered mode of actin-dependent uptake. We therefore propose the model (Figure 7) that it is the incomplete clathrin structure formed during VSV uptake that elicits the actin-based response to rescue the endocytic process and leads to the successful engulfment of the trapped virus particle.

Actin-dependent clathrin-mediated endocytosis

The importance of actin function during clathrin-mediated endocytosis varies. In yeast cells, actin polymerization drives invagination and endocytosis of long-lived (>2 min.) clathrin assemblies through tubular intermediates with clathrin at the cytosolic tip [33–35]. Mammalian cells also form large (0.2–1 μm), relatively flat arrays of clathrin, or 'plaques,' on the adherent cell surface [26,36]. These structures also exhibit long lifetimes (2-15+ min.) and require local actin assembly for internalization [26]. Coated pit internalization from the apical (but not the basolateral) surface of polarized mammalian cells [37,38] and lamprey neuronal synapses [39,40] is also actin-dependent. By contrast, actin polymerization is only required for the uptake of clathrin

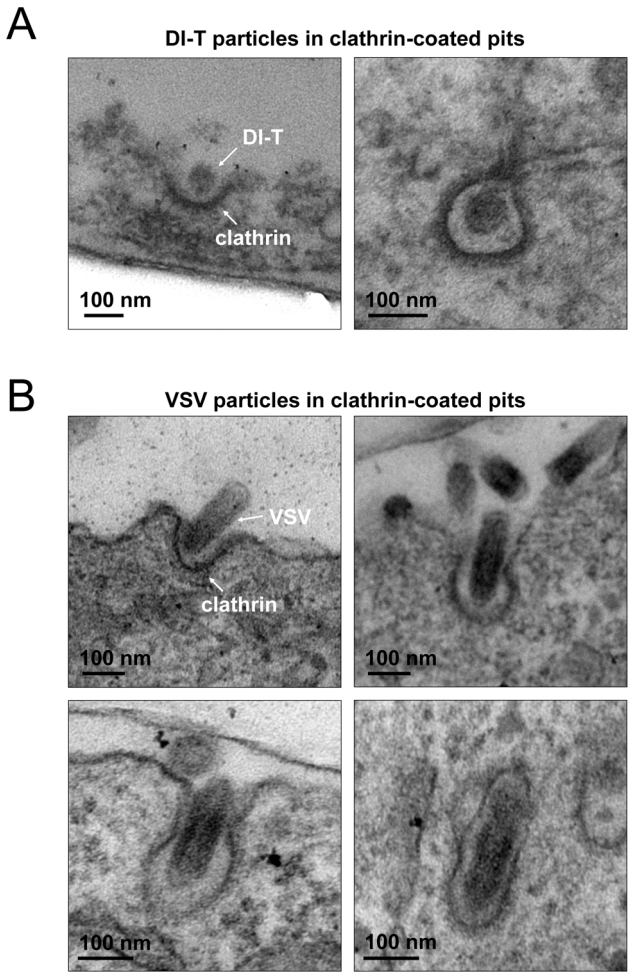

Figure 4. Electron microscopic images of DI-T and VSV particles in clathrin-coated pits. (A) Electron micrographs depicting DI-T particles at early (left) or late (right) stages of clathrin-dependent endocytosis. BSC1 cells were incubated with ~1000 particles per cell for 10 min. at 37°C. Cells were then fixed, and samples were processed for ultra thin sectioning and viewed as described in the materials and methods. (B) Electron micrographs of VSV particles at sequential (left to right, top to bottom) stages of clathrin-dependent endocytosis. Vero cells were inoculated with VSV at an MOI of 5, and samples were prepared for analysis at 6 h post-infection.
doi:10.1371/journal.ppat.1001127.g004

plaques and not conventional coated pits in several types of nonpolarized mammalian cells [26,41]. Thus, while actin dynamics play an evolutionarily conserved role in clathrin-dependent endocytosis, mammalian cells regulate the interplay between the clathrin and actin systems.

Our analyses of VSV and coated plaque internalization reveal two properties that correlate with their actin-dependent uptake mechanisms. First, plaques and VSV-containing structures remain on the plasma membrane for >2-fold longer than standard coated pits [15,26] (Figure 3C, E). The prolonged presence of a clathrin lattice might promote interactions between clathrin-associated proteins and regulators of actin polymerization. Second, clathrin plaques and VSV-containing structures physically differ from standard coated pits. Plaques fail to constrict their outer boundaries during the final phase of clathrin assembly [26], and pits containing VSV lack a complete clathrin coat [15,17]. Such unusual structural features might attract proteins that associate with exposed lipids, such as dynamin. Indeed, significantly more dynamin molecules accumulate during the final stages of VSV uptake [15]. This localized increase in dynamin may enhance the recruitment of dynamin-interacting proteins with the capacity to bind lipids and activate the Arp2/3 complex through N-WASP, including endophilin, syndapin, and SNX9 [42–46]. Although these proteins may link the clathrin and actin systems and facilitate localized membrane remodeling during endocytosis (reviewed in [47]), further studies are needed to determine whether they play a role in clathrin-dependent VSV endocytosis. Comparative studies of VSV and DI-T uptake may provide a useful tool to dissect the mechanisms that regulate actin assembly during clathrin-mediated endocytosis.

Implications for the internalization mechanisms of other viruses

The dimensions of the actin-dependent VSV particle and the actin-independent DI-T particle fall within the range of shapes present in many pleomorphic viruses. Our work suggests that this may lead to important distinctions in their mode of uptake. For example, some influenza A virus strains, such as X-31, produce spherical particles that measure 80–120 nm in diameter [18]. By contrast, the Udorn strain forms filamentous particles that measure 80–100 nm wide and up to 30 microns in length [48,49]. Although influenza A virus can enter cells by clathrin-dependent and -independent mechanisms [14], the impact of particle shape on the entry pathway remains unknown. It seems likely that remodeling of the cortical actin cytoskeleton will be important for uptake of filamentous influenza particles, and clathrin may facilitate local membrane deformation during the endocytic process. The *Arenaviridae* generate roughly spherical particles that range in diameter from 40–300 nm [50,51], and it is known that clathrin function is important for efficient infection of cells by some New World arenaviruses [52]. It will now be of interest to determine whether spherical particles of different diameter employ altered modes of clathrin-based endocytosis.

Pseudotyping is often used to study the entry pathway of highly pathogenic viruses, including the long filamentous filoviruses, Ebola and Marburg, as well as several arenaviruses. Such pseudotypes are frequently based on VSV or retroviral virions in which the endogenous entry proteins have been replaced with the surface glycoproteins of the pathogenic virus [53–56]. Although viral pseudotypes are useful for studying the entry process, VSV and the spherical virions of retroviruses (~100 nm in diameter) do not accurately recapitulate the sizes or shapes of the pleomorphic viruses. Our studies of VSV and DI-T clearly show that virion geometry can fundamentally alter aspects of the viral internalization process. Therefore, it is critically important to study viral endocytosis using pseudotyped or virus-like particles that closely approximate the physical properties of a virus in question.

Materials and Methods

Cells and viruses

African green monkey kidney BS-C-1 cells (herein BSC1, American Type Culture Collection (ATCC) CCL-26; Manassas, VA) and Vero cells (ATCC) were maintained at 37°C and 5% CO_2 in Dulbecco's Modified Eagle Medium (DMEM, Invitrogen Corporation; Carlsbad, CA) supplemented with 10% fetal bovine serum (Tissue Culture Biologicals; Tulare, CA). BSC1 cells stably expressing rat σ2 adaptin-eGFP (σ2-eGFP) [9] were maintained as above in the presence of 0.4 mg mL^{-1} geneticin (G418, Invitrogen).

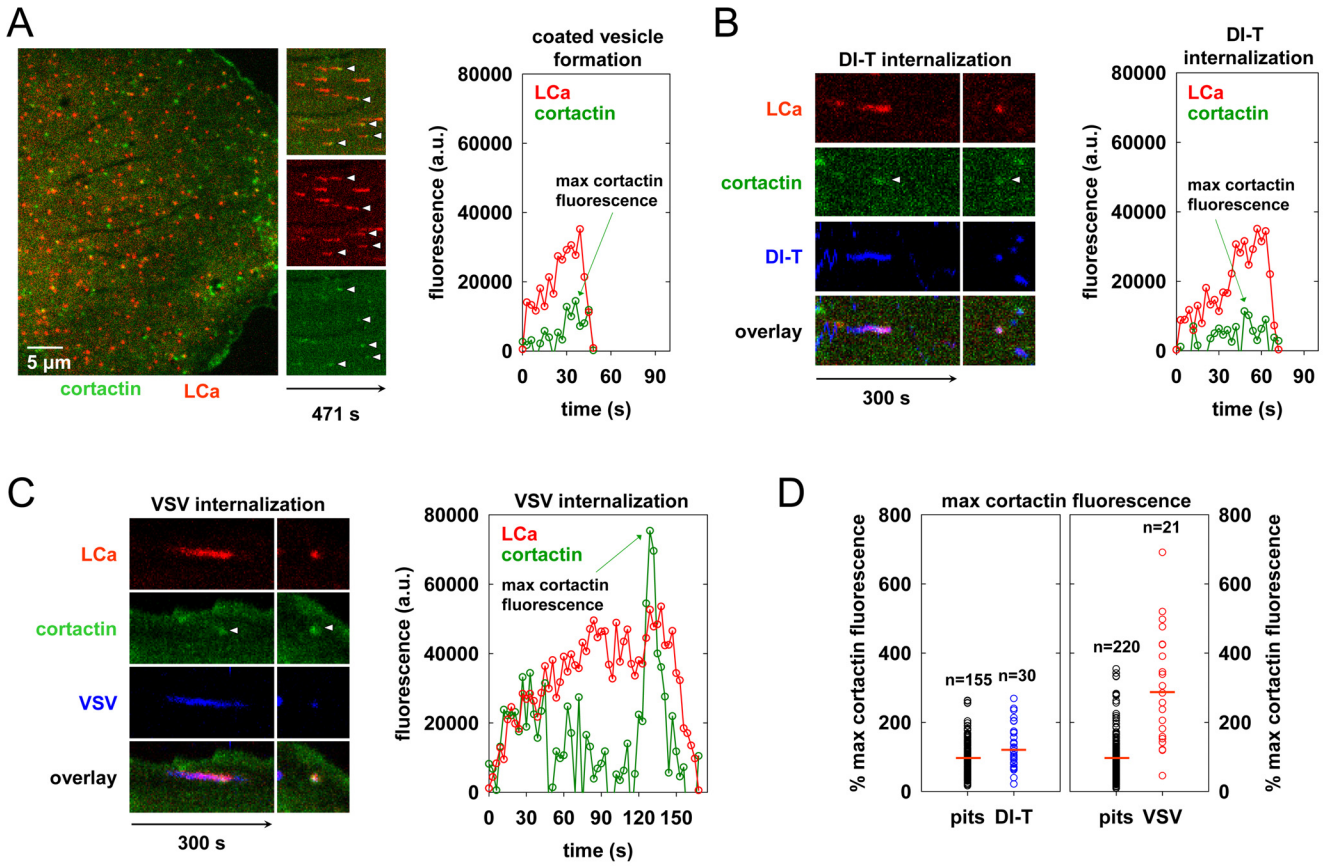

Figure 5. Clathrin structures containing VSV recruit more cortactin that pits that internalize DI-T. (A) Cortactin recruitment during coated pit formation. Left, snapshot showing the surface of a BSC1 cell transiently expressing cortactin-eGFP (green) and mCherry-LCa (red) at 18 h post-transfection. Time-lapse images were acquired at 3 s intervals, and frame 83 is shown. Middle, split channel kymographs of coated pit formation in the cell at left. White arrowheads highlight pits in which cortactin recruitment is clearly visible above the local background. Right, example plot of cortactin and clathrin fluorescence intensity over time during the formation of a single clathrin-coated pit in the cell shown at left (Video S5). (B and C) Examples of cortactin recruitment during DI-T (B) and VSV (C) uptake. BSC1 cells transiently expressing mCherry-LCa (red) and cortactin-eGFP (green) were inoculated with Alexa Fluor 647-labeled DI-T or VSV, and images were acquired as in A. Left, split-channel kymograph views of protein and virion (blue) fluorescence intensity over time (Videos S6, S7). Images in the right-hand panels show a snapshot of the maximal cortactin or clathrin fluorescence, and white arrowheads highlight the peak cortactin signal. Right, plots of the cortactin and clathrin fluorescence intensity over time for each internalization event. (D) Relative peak fluorescence intensity of cortactin in cells co-expressing mCherry-LCa and cortactin-eGFP. At 18 h post-transfection, samples were separately inoculated with DI-T or VSV particles, and images were acquired as in A. For each cell that was imaged, the maximum cortactin fluorescence associated with ~50 pits lacking virus particles (pits, black) and all pits that internalized a DI-T (left, blue, 3 cells) or VSV (right, red, 5 cells) particle was measured. The data are plotted as described in the legend of Figure 3C, and the number of events is shown above each plot. Numerical values and statistical analyses are provided in Table 1.
doi:10.1371/journal.ppat.1001127.g005

Recombinant VSV (rVSV) [25] was amplified and purified as before [15]. Defective interfering T (DI-T) particles of VSV were recovered from a cDNA clone of the DI-T genome [24]. The DI-T particles were amplified by co-infecting baby hamster kidney cells (BHK-21, ATCC C-13) with rVSV (multiplicity of infection (MOI) 50). A subsequent passage was performed by inoculating cells with filtered, undiluted supernatant from the primary amplification and rVSV (MOI of 50). Viruses were concentrated by centrifugation at 44,000× g, and the virus pellet was resuspended in NTE (10 mM Tris pH 7.4, 100 mM NaCl, 1 mM EDTA). The two particle forms were separated on a 15–45% sucrose gradient prepared in NTE by centrifugation at 77,000× g for 5 h. The DI-T particles were extracted from the upper virus band, concentrated as before, and resuspended to 1 mg mL^{-1} of total protein in PBS.

Dye conjugation to virus particles

Purified DI-T and VSV particles were labeled with Alexa Fluor dye molecules (Molecular Probes, Invitrogen) as previously described [15] except that the final dye concentration in the labeling reaction was reduced to 25 µg ml^{-1}. Plaque assays of virus preps before and after labeling showed that dye conjugation did not affect the infectivity of VSV particles or the capacity of DI-T virions to inhibit plaque formation by VSV. The surface density of G protein on VSV or DI-T particles was estimated by measuring the ratio of G protein to N protein in each particle population. To separate and visualize the viral proteins, purified virions were subjected to SDS-PAGE using 10% polyacrylamide and 0.13% bis-acrylamide and stained with Coomassie blue. The relative amounts of N or G protein were established using ImageJ (U. S. National Institutes of Health, Bethesda, Maryland; http://rsb.info.nih.gov/ij/).

Nucleic acid transfection

BSC1 cells were seeded into 6-well plates at ~60,000 cells per well 16–20 h prior to transfection. Plasmid DNA was introduced into the cells using FuGENE 6 (Roche Diagnostics; Indianapolis,

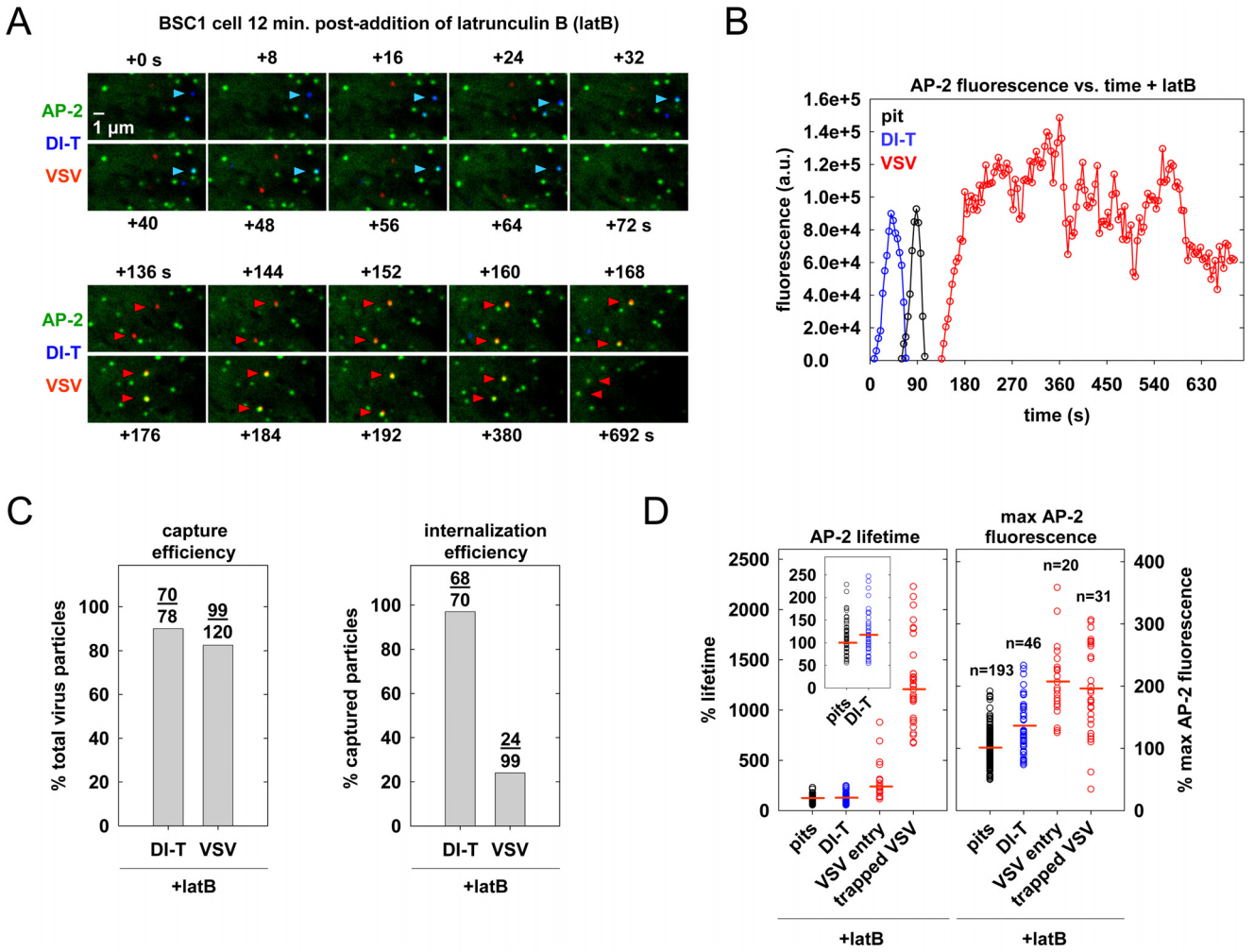

Figure 6. Actin polymerization is not required for DI-T internalization. (A) The endocytic fate of virus particles after inhibition of actin polymerization. BSC1 cells stably expressing σ2-eGFP (green) were treated with 6.3 µM latB for 12 min. and inoculated with DI-T and VSV particles in the continued presence of latB. Time-lapse images of a single cell were acquired at 4 s intervals for 692 s, and an 8.8×5.0 µm^2 area of the cell surface is shown. The upper panels show the complete internalization of a DI-T particle (blue, blue arrowheads), where +0 s indicates the first frame of the time-lapse series. The lower panels show the subsequent capture but failed internalization of 2 VSV (red, red arrowheads) particles on the same area of cell membrane (time scale continued from above) (Video S8). (B) AP-2 fluorescence intensity for the events shown in A. Note that the adaptor fluorescence associated with the DI-T particle (blue) and a conventional coated pit (black) that formed within the same membrane area peak and disappear normally, while the adaptor signal associated with the upper-most VSV particle (red) does not, signifying failed internalization. (C) Effect of latB on the efficiency of virus capture and internalization. BSC1 cells stably expressing σ2-eGFP were treated and imaged as described in A. Left, the percentage of virus particles that were captured by a clathrin structure after attachment. Right, the percentage of captured virus particles that were successfully internalized within 300 s of capture (see D. for details). Cumulative data are from 5 cells. (D) Effect of latB on the lifetime and peak fluorescence intensity of AP-2 in clathrin structures. Data were acquired as described in A. and displayed as in the legend of Figure 3C. Left, relative lifetime of AP-2 in structures that lack (pits, black) or capture a virus particle. Inset shows a rescaled distribution of the pit and DI-T internalization events. Right, maximum fluorescence intensity of AP-2 in the events at left. Data are from 4 of the 5 cells analyzed in C, as thermal drift during imaging prevented accurate fluorescence intensity measurements in one cell. The number of events in each category is shown above the corresponding plots at right. DI-T (blue) data consists only of productive internalization events. VSV events are categorized as productive internalizations (VSV entry, red) or non-productive captures (trapped VSV, red). A non-productive capture is defined as a stable colocalization between a spot of AP-2 and a VSV particle that began at least 300 s before the last captured image and did not result in virus uptake before cessation of imaging. The 300 s cutoff was chosen because a majority (22/24) of productive internalizations occurred within 300 s of capture. Captures in which the final image frame was acquired before 300 s elapsed were excluded from the analysis, as the eventual endocytic fate of the particle cannot be predicted.

doi:10.1371/journal.ppat.1001127.g006

IN) according to the manufacturer's instructions. Prior to transfection, media on the cells was replaced with 1 ml OPTIMEM (Invitrogen). After addition of the transfection mixture, cells were incubated at 37°C for 5 h, and the existing media was supplemented with 2 ml DMEM containing 10% FBS. To ensure optimal replacement of endogenous clathrin light chain molecules with rat eGFP-clathrin light chain A1 (eGFP-LCa) [9], cells were transfected with 0.75 µg of plasmid DNA encoding eGFP-LCa. The cells were cultured for ~36 h and seeded onto glass coverslips ~14 h prior to image acquisition. Co-expression of mCherry-LCa (constructed as described for tomato-LCa [8]) and mouse cortactin-eGFP [57,58] was achieved by transfection of cells on glass coverslips with 1 µg of each plasmid, and the cells were imaged ~18 h later.

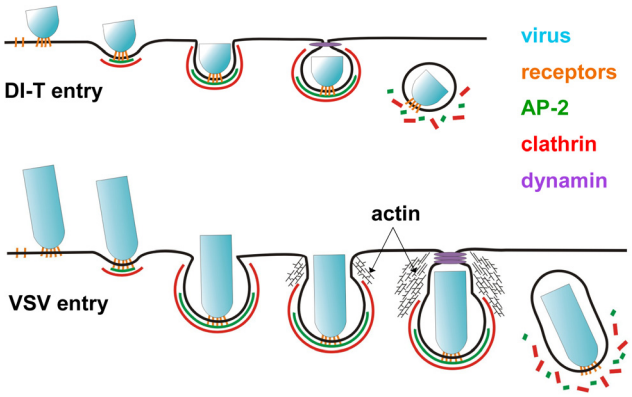

Figure 7. Model of DI-T and VSV entry. DI-T (above) and VSV (below) particles engage host cells through interactions between the viral surface glycoproteins and unknown cellular receptor moieties. Following attachment, both particle types undergo slow diffusion (diffusion coefficient $\sim 5\times10^{-11}$ cm^2 s^{-1}) on the cell surface for an average of ~2 min. before being captured by a clathrin-coated pit. For DI-T, continued clathrin assembly drives complete particle envelopment by the plasma membrane and leads to virus endocytosis. In contrast, the presence of a VSV particle in a coated pit physically prevents complete membrane constriction by the clathrin machinery and causes clathrin assembly to halt prematurely. The force provided by actin polymerization then further remodels the plasma membrane and thereby encloses the virus particle in a partially clathrin-coated vesicle.
doi:10.1371/journal.ppat.1001127.g007

Live cell imaging

Cells on 25 mm coverslips (No. 1.5, Electron Microscopy Sciences; Hatfield, PA) were placed into a perfusion chamber and overlaid with α-MEM lacking phenol red (Invitrogen) and supplemented with 20 mM HEPES pH 7.4 and 2% FBS. The chamber was placed in a heated sample holder (20/20 Technology Inc.; Wilmington, NC) mounted on the stage of a Mariana imaging system (Intelligent Imaging Innovations, Denver, CO) based on an Axiovert 200M inverted microscope (Carl Zeiss, Inc.; Thornwood, NY). The microscope stage and objective lenses were maintained at 37°C within an environmental chamber, and the air above the cells was supplied with 5% CO_2. The position of the sample holder with respect to the objective lens was manipulated using a PZ-2000 automated stage (Applied Scientific Instrumentation; Eugene, OR). Samples were illuminated using 40–50 mW solid state lasers ($\lambda = 488$, Coherent, Inc.; Santa Clara, CA, $\lambda = 561$, Cobolt AB; Solna, Sweden, $\lambda = 640$, 40 mW; Coherent) directed through an acousto-optic tunable filter (AOTF; Gooch and Housego L.L.C.; Melbourne, FL). Laser illumination was imparted on the sample through a CSU-X1 spinning disk confocal unit (Yokogawa Electric Corporation; Tokyo, Japan) and a 63X objective lens (Plan-Apochromat, NA 1.4, Carl Zeiss). Emission spectra were selected using single band width emission filters (LF405/488/561/635-A, Semrock; Rochester, NY), and after transmission through a spherical aberration correction device (Infinity Photo-Optical; Boulder, CO), the emission photons were collected using a Cascade II:512B back-illuminated EMCCD camera (Roper Scientific, Photometrics; Tuscon, AZ). Under this configuration, a single pixel corresponds to 0.07×0.07 μm^2. Slidebook 4.2.13 (Intelligent Imaging Innovations, Inc. (III); Denver, CO) was used to command the hardware devices and visualize the acquired data.

To image virus internalization, Alexa-labeled virus was centrifuged briefly to remove aggregates, and cells were inoculated with virus to result in attachment of <50 particles per cell within 20 min. (~1×10^7 p.f.u. of VSV, ~MOI 100, 0.005–0.05 particles per μm^2 of cell surface area). Time-lapse acquisitions were typically carried out for 8–10 min. per cell, and images were captured at 3–4 s intervals after sequentially illuminating the sample with the appropriate laser for 50–100 ms per wavelength. To assess the effect of latrunculin B (latB) (Sigma-Aldrich, Inc.; St. Louis, MO) on coated vesicle formation and virus entry, cells were treated with 6.3 μM of latB for ~10 min. at 37°C prior to the addition of virus particles.

Image analysis

Image analysis was performed as previously described [15] with the following modifications. Slidebook 4.2.13 (III) was used to view, scale, and export images for publication. Movies were generated by exporting a series of continuous TIFF files from a Slidebook time-lapse acquisition and compiling the images into a single AVI file using ImageJ (NIH). SigmaPlot 8.0 (SYSTAT; Point Richmond, CA) was used to plot data. Microsoft Excel was used to determine whether data from 2 categories differ in a statistically significant manner using two-tailed Student's t-tests. An automated image analysis application (IMAB) [8] developed within MATLAB (Mathworks; Natick, MA) was used to track the formation of clathrin-coated structures and the internalization of single virus particles. Images were processed for analysis as previously described, and established criteria were used to exclude incomplete endocytic events and events in which pixels assigned to one clathrin structure merged with or split from an adjacent structure [8]. For each cell of interest, the first ~50 pits lacking virus particles were analyzed in detail to measure the coat lifetime and protein composition (see below). All complete virus uptake events that occurred in these cells were also analyzed in a similar manner. With the exception of internalization events blocked by latB, incomplete internalization events or events truncated by the start/end of image acquisition were not analyzed. Aggregates of virus were identified as objects with fluorescence intensities greater than that of single particles and were excluded from all analyses.

IMAB was used to measure the fluorescence intensity of coat components or virus particles in the following manner. A roughly spherical mask encompassing 69 pixels was centered on the peak fluorescence intensity of the object in all frames that the object was detectable above the local background fluorescence. The contribution of the local background fluorescence was estimated by measuring the average intensity of pixels within a ring of single pixel width that extended from the outer boundary of the object mask. The intensity of the pixels within the object mask was then summed, and the average intensity value of pixels in the local background was subtracted from each pixel within the object mask to estimate the fluorescence contributed by proteins (or dye molecules) within the object of interest.

Electron microscopy

Purified virus particles were deposited onto carbon-coated copper grids and stained with 2% phosphotungstic acid (PTA) in H_2O (pH 7.5). To visualize DI-T particles in clathrin-coated pits, BSC1 cells were inoculated with unlabeled DI-T particles using a dose that yielded ~1000 attached particles per cell after 10 min. Samples were then processed for ultra-thin sectioning as previously described [15,59]. Electron micrographs of VSV particles in clathrin endocytic structures were obtained from cells infected with VSV for 6 h, where the entry of newly released particles could readily be visualized. Virus particles and ultra-thin sections of cells were viewed using a Tecnai G^2 Spirit BioTWIN transmission electron microscope (FEI, Hillsboro, OR).

Supporting Information

Video S1 Clathrin-dependent DI-T internalization. BSC1 cells stably expressing σ2-eGFP (green) were inoculated with DI-T particles, and time-lapse images were acquired at 4 s intervals. A 4.2×4.2 μm^2 area of the cell surface is shown as in Figure 2B. The video depicts a single DI-T particle (red) that attaches to the plasma membrane and diffuses slowly. A clathrin-coated pit captures the virus particle when a dim adaptor spot colocalizes with the virus signal. The adaptor fluorescence intensity increases as coated pit assembly proceeds, and particle internalization occurs shortly after the adaptor signal peaks. Disappearance of the adaptor signal signifies clathrin uncoating, and the virus-containing vesicle is then transported toward the cell interior.
Found at: doi:10.1371/journal.ppat.1001127.s001 (0.31 MB AVI)

Video S2 Sequential internalization of single VSV and DI-T particles by the same cell. BSC1 cells stably expressing σ2-eGFP (green) were simultaneously inoculated with wild-type VSV and DI-T particles, and time-lapse images were acquired at 4 s intervals. A 3.5×3.5 μm^2 area of the cell surface is shown as in Figure 3A. At the outset of imaging (t = 0), one VSV (red) particle and one DI-T particle (blue) are visible on the cell surface. The VSV particle enters first, followed by the DI-T particle.
Found at: doi:10.1371/journal.ppat.1001127.s002 (0.39 MB AVI)

Video S3 Uptake of a single DI-T particle by a cell expressing eGFP-LCa. BSC1 cells transiently expressing eGFP-LCa were inoculated with DI-T and full-length VSV particles, and images were captured as for Video S2. At the onset of imaging, a DI-T particle is present within a 3.5×3.5 μm^2 area of the cell surface. Shortly thereafter, the particle briefly colocalizes with a spot of eGFP-LCa but does not enter. As visualized in Figure 3B, a clathrin-coated pit subsequently initiates near the virion, and the particle disappears into the cell after the clathrin signal peaks.
Found at: doi:10.1371/journal.ppat.1001127.s003 (0.77 MB AVI)

Video S4 Uptake of a single VSV particle by a cell expressing eGFP-LCa. The movie depicts a separate area (of equal size) of the plasma membrane from the same cell that internalized the particle shown in Video S3. A VSV particle (red) attaches to the cell surface, and a clathrin endocytic structure subsequently internalizes the particle (Figure 3D).
Found at: doi:10.1371/journal.ppat.1001127.s004 (0.77 MB AVI)

Video S5 Cortactin recruitment during conventional clathrin-coated pit formation. Time-lapse images were acquired at 3 s intervals from a cell transiently co-expressing mCherry-LCa (red) and cortactin-eGFP (green) (Figure 5A). A 7.0×7.0 μm^2 area of the cell surface is shown. Note that the cortactin signal is nearly indistinguishable from the local background during most clathrin endocytic events.
Found at: doi:10.1371/journal.ppat.1001127.s005 (3.01 MB AVI)

Video S6 Cortactin recruitment during the internalization of a single DI-T particle. BSC1 cells transiently co-expressing mCherry-LCa (red) and cortactin-eGFP (green) for 18 h were inoculated with DI-T particles (blue), and time-lapse images were acquired at 3 s intervals. The video shows the internalization of a single DI-T particle by a clathrin-coated vesicle. The internalization event is centered within a 3.5×3.5 μm^2 area of the cellular plasma membrane (Figure 5B). The left panel shows an overlay of the 3 channels, and the right panel shows only the cortactin channel displayed in monochrome. Note that the cortactin fluorescence intensity during DI-T entry is nearly indistinguishable from the local background.
Found at: doi:10.1371/journal.ppat.1001127.s006 (1.42 MB AVI)

Video S7 Cortactin recruitment during the internalization of a wild-type VSV particle. BSC1 cells transiently co-expressing mCherry-LCa (red) and cortactin-eGFP (green) for 18 h were inoculated with VSV particles (blue), and time-lapse images were acquired at 3 s intervals. The video is displayed as described for Video S3 and shows the clathrin-dependent uptake of a single VSV particle in a 3.5×3.5 μm^2 area of the plasma membrane (Figure 5C). Note the visible burst of cortactin that occurs in the final stages of VSV internalization.
Found at: doi:10.1371/journal.ppat.1001127.s007 (1.51 MB AVI)

Video S8 BSC1 cells stably expressing σ2-eGFP were treated with 6.3 μM latB for 12 min. Cells were inoculated with DI-T (blue) and VSV (red) particles, and images were acquired at 4 s intervals. The movie shows an 8.8×5.0 μm^2 area of the plasma membrane. The 2 DI-T particles (the lower particle is already in a coated pit at the onset of imaging) enter in the presence of latB, while the 2 VSV particles are subsequently captured by coated pits but fail to enter the cell (Figure 6A, B).
Found at: doi:10.1371/journal.ppat.1001127.s008 (4.65 MB AVI)

Acknowledgments

We express gratitude to Eric Marino for maintaining the imaging resource used in this study. We also gratefully acknowledge Maria Ericsson and Irene Kim for preparation of samples for electron microscopic analysis and members of the Kirchhausen and Whelan labs for thought-provoking discussions.

Author Contributions

Conceived and designed the experiments: DKC RHM SPJW TK. Performed the experiments: DKC. Analyzed the data: DKC SPJW TK. Contributed reagents/materials/analysis tools: DKC RHM SPJW TK. Wrote the paper: DKC SPJW TK.

References

1. Conner SD, Schmid SL (2003) Regulated portals of entry into the cell. Nature 422: 37–44.
2. Kirchhausen T (2000) Clathrin. Annu Rev Biochem 69: 699–727.
3. Kirchhausen T (2009) Imaging endocytic clathrin structures in living cells. Trends Cell Biol 19: 596–605.
4. Owen DJ, Evans PR (1998) A structural explanation for the recognition of tyrosine-based endocytotic signals. Science 282: 1327–1332.
5. Honing S, Ricotta D, Krauss M, Spate K, Spolaore B, et al. (2005) Phosphatidylinositol-(4,5)-bisphosphate regulates sorting signal recognition by the clathrin-associated adaptor complex AP2. Mol Cell 18: 519–531.
6. Damke H, Baba T, Warnock DE, Schmid SL (1994) Induction of mutant dynamin specifically blocks endocytic coated vesicle formation. J Cell Biol 127: 915–934.
7. Lee DW, Zhao X, Zhang F, Eisenberg E, Greene LE (2005) Depletion of GAK/auxilin 2 inhibits receptor-mediated endocytosis and recruitment of both clathrin and clathrin adaptors. J Cell Sci 118: 4311–4321.
8. Massol RH, Boll W, Griffin AM, Kirchhausen T (2006) A burst of auxilin recruitment determines the onset of clathrin-coated vesicle uncoating. Proc Natl Acad Sci U S A 103: 10265–10270.
9. Ehrlich M, Boll W, Van Oijen A, Hariharan R, Chandran K, et al. (2004) Endocytosis by random initiation and stabilization of clathrin-coated pits. Cell 118: 591–605.
10. Loerke D, Mettlen M, Yarar D, Jaqaman K, Jaqaman H, et al. (2009) Cargo and dynamin regulate clathrin-coated pit maturation. PLoS Biol 7: e57.
11. Hanover JA, Beguinot L, Willingham MC, Pastan IH (1985) Transit of receptors for epidermal growth factor and transferrin through clathrin-coated pits. Analysis of the kinetics of receptor entry. J Biol Chem 260: 15938–15945.
12. Anderson RG, Brown MS, Goldstein JL (1977) Role of the coated endocytic vesicle in the uptake of receptor-bound low density lipoprotein in human fibroblasts. Cell 10: 351–364.

13. van der Schaar HM, Rust MJ, Chen C, van der Ende-Metselaar H, Wilschut J, et al. (2008) Dissecting the cell entry pathway of dengue virus by single-particle tracking in living cells. PLoS Pathog 4: e1000244.
14. Rust MJ, Lakadamyali M, Zhang F, Zhuang X (2004) Assembly of endocytic machinery around individual influenza viruses during viral entry. Nat Struct Mol Biol 11: 567–573.
15. Cureton DK, Massol RH, Saffarian S, Kirchhausen TL, Whelan SP (2009) Vesicular stomatitis virus enters cells through vesicles incompletely coated with clathrin that depend upon actin for internalization. PLoS Pathog 5: e1000394.
16. Veiga E, Guttman JA, Bonazzi M, Boucrot E, Toledo-Arana A, et al. (2007) Invasive and adherent bacterial pathogens co-Opt host clathrin for infection. Cell Host Microbe 2: 340–351.
17. Simpson RW, Hauser RE, Dales S (1969) Viropexis of vesicular stomatitis virus by L cells. Virology 37: 285–290.
18. Harris A, Cardone G, Winkler DC, Heymann JB, Brecher M, et al. (2006) Influenza virus pleiomorphy characterized by cryoelectron tomography. Proc Natl Acad Sci U S A 103: 19123–19127.
19. Meier E, Harmison GG, Keene JD, Schubert M (1984) Sites of copy choice replication involved in generation of vesicular stomatitis virus defective-interfering particle RNAs. J Virol 51: 515–521.
20. Huang AS, Wagner RR (1966) Defective T particles of vesicular stomatitis virus. II. Biologic role in homologous interference. Virology 30: 173–181.
21. Peng G, Tsao J, Schein S, Green TJ, Luo M, et al. (2010) Cryo-EM model of the bullet-shaped vesicular stomatitis virus. Science 327: 689–693.
22. Huang AS, Greenawalt JW, Wagner RR (1966) Defective T particles of vesicular stomatitis virus. I. Preparation, morphology, and some biologic properties. Virology 30: 161–172.
23. Wagner RR, Schnaitman TA, Snyder RM (1969) Structural proteins of vesicular stomatitis viruses. J Virol 3: 395–403.
24. Pattnaik AK, Ball LA, LeGrone AW, Wertz GW (1992) Infectious defective interfering particles of VSV from transcripts of a cDNA clone. Cell 69: 1011–1020.
25. Whelan SP, Ball LA, Barr JN, Wertz GT (1995) Efficient recovery of infectious vesicular stomatitis virus entirely from cDNA clones. Proc Natl Acad Sci U S A 92: 8388–8392.
26. Saffarian S, Cocucci E, Kirchhausen T (2009) Distinct dynamics of endocytic clathrin-coated pits and coated plaques. PLoS Biol 7: e1000191.
27. Uruno T, Liu J, Zhang P, Fan Y, Egile C, et al. (2001) Activation of Arp2/3 complex-mediated actin polymerization by cortactin. Nat Cell Biol 3: 259–266.
28. McNiven MA, Kim L, Krueger EW, Orth JD, Cao H, et al. (2000) Regulated interactions between dynamin and the actin-binding protein cortactin modulate cell shape. J Cell Biol 151: 187–198.
29. Merrifield CJ, Perrais D, Zenisek D (2005) Coupling between clathrin-coated-pit invagination, cortactin recruitment, and membrane scission observed in live cells. Cell 121: 593–606.
30. Coue M, Brenner SL, Spector I, Korn ED (1987) Inhibition of actin polymerization by latrunculin A. FEBS Lett 213: 316–318.
31. Coyne CB, Bergelson JM (2006) Virus-induced Abl and Fyn kinase signals permit coxsackievirus entry through epithelial tight junctions. Cell 124: 119–131.
32. Coyne CB, Kim KS, Bergelson JM (2007) Poliovirus entry into human brain microvascular cells requires receptor-induced activation of SHP-2. Embo J 26: 4016–4028.
33. Kaksonen M, Toret CP, Drubin DG (2006) Harnessing actin dynamics for clathrin-mediated endocytosis. Nat Rev Mol Cell Biol 7: 404–414.
34. Kaksonen M, Sun Y, Drubin DG (2003) A pathway for association of receptors, adaptors, and actin during endocytic internalization. Cell 115: 475–487.
35. Idrissi FZ, Grotsch H, Fernandez-Golbano IM, Presciatto-Baschong C, Riezman H, et al. (2008) Distinct acto/myosin-I structures associate with endocytic profiles at the plasma membrane. J Cell Biol 180: 1219–1232.
36. Heuser J (1980) Three-dimensional visualization of coated vesicle formation in fibroblasts. J Cell Biol 84: 560–583.
37. Gottlieb TA, Ivanov IE, Adesnik M, Sabatini DD (1993) Actin microfilaments play a critical role in endocytosis at the apical but not the basolateral surface of polarized epithelial cells. J Cell Biol 120: 695–710.
38. Da Costa SR, Sou E, Xie J, Yarber FA, Okamoto CT, et al. (2003) Impairing actin filament or syndapin functions promotes accumulation of clathrin-coated vesicles at the apical plasma membrane of acinar epithelial cells. Mol Biol Cell 14: 4397–4413.
39. Shupliakov O, Bloom O, Gustafsson JS, Kjaerulff O, Low P, et al. (2002) Impaired recycling of synaptic vesicles after acute perturbation of the presynaptic actin cytoskeleton. Proc Natl Acad Sci U S A 99: 14476–14481.
40. Bourne J, Morgan JR, Pieribone VA (2006) Actin polymerization regulates clathrin coat maturation during early stages of synaptic vesicle recycling at lamprey synapses. J Comp Neurol 497: 600–609.
41. Boucrot E, Saffarian S, Massol R, Kirchhausen T, Ehrlich M (2006) Role of lipids and actin in the formation of clathrin-coated pits. Exp Cell Res 312: 4036–4048.
42. Qualmann B, Roos J, DiGregorio PJ, Kelly RB (1999) Syndapin I, a synaptic dynamin-binding protein that associates with the neural Wiskott-Aldrich syndrome protein. Mol Biol Cell 10: 501–513.
43. Soulet F, Yarar D, Leonard M, Schmid SL (2005) SNX9 regulates dynamin assembly and is required for efficient clathrin-mediated endocytosis. Mol Biol Cell 16: 2058–2067.
44. Yarar D, Waterman-Storer CM, Schmid SL (2007) SNX9 couples actin assembly to phosphoinositide signals and is required for membrane remodeling during endocytosis. Dev Cell 13: 43–56.
45. Ringstad N, Nemoto Y, De Camilli P (1997) The SH3p4/Sh3p8/SH3p13 protein family: binding partners for synaptojanin and dynamin via a Grb2-like Src homology 3 domain. Proc Natl Acad Sci U S A 94: 8569–8574.
46. Otsuki M, Itoh T, Takenawa T (2003) Neural Wiskott-Aldrich syndrome protein is recruited to rafts and associates with endophilin A in response to epidermal growth factor. J Biol Chem 278: 6461–6469.
47. Dawson JC, Legg JA, Machesky LM (2006) Bar domain proteins: a role in tubulation, scission and actin assembly in clathrin-mediated endocytosis. Trends Cell Biol 16: 493–498.
48. Roberts PC, Compans RW (1998) Host cell dependence of viral morphology. Proc Natl Acad Sci U S A 95: 5746–5751.
49. Roberts PC, Lamb RA, Compans RW (1998) The M1 and M2 proteins of influenza A virus are important determinants in filamentous particle formation. Virology 240: 127–137.
50. Neuman BW, Adair BD, Burns JW, Milligan RA, Buchmeier MJ, et al. (2005) Complementarity in the supramolecular design of arenaviruses and retroviruses revealed by electron cryomicroscopy and image analysis. J Virol 79: 3822–3830.
51. Murphy FA, Webb PA, Johnson KM, Whitfield SG, Chappell WA (1970) Arenoviruses in Vero cells: ultrastructural studies. J Virol 6: 507–518.
52. Rojek JM, Sanchez AB, Nguyen NT, de la Torre JC, Kunz S (2008) Different mechanisms of cell entry by human-pathogenic Old World and New World arenaviruses. J Virol 82: 7677–7687.
53. Chandran K, Sullivan NJ, Felbor U, Whelan SP, Cunningham JM (2005) Endosomal proteolysis of the Ebola virus glycoprotein is necessary for infection. Science 308: 1643–1645.
54. Negrete OA, Levroney EL, Aguilar HC, Bertolotti-Ciarlet A, Nazarian R, et al. (2005) EphrinB2 is the entry receptor for Nipah virus, an emergent deadly paramyxovirus. Nature 436: 401–405.
55. Clemente R, de la Torre JC (2009) Cell entry of Borna disease virus follows a clathrin-mediated endocytosis pathway that requires Rab5 and microtubules. J Virol 83: 10406–10416.
56. Bhattacharyya S, Warfield KL, Ruthel G, Bavari S, Aman MJ, et al. (2010) Ebola virus uses clathrin-mediated endocytosis as an entry pathway. Virology 401: 18–28.
57. Le Clainche C, Pauly BS, Zhang CX, Engqvist-Goldstein AE, Cunningham K, et al. (2007) A Hip1R-cortactin complex negatively regulates actin assembly associated with endocytosis. Embo J 26: 1199–1210.
58. Kaksonen M, Peng HB, Rauvala H (2000) Association of cortactin with dynamic actin in lamellipodia and on endosomal vesicles. J Cell Sci 113 Pt 24: 4421–4426.
59. Maupin P, Pollard TD (1983) Improved preservation and staining of HeLa cell actin filaments, clathrin-coated membranes, and other cytoplasmic structures by tannic acid-glutaraldehyde-saponin fixation. J Cell Biol 96: 51–62.